IRIS AperTO

UNIVERSITÀ DEGLI STUDI DI TORINO

AperTO - Archivio Istituzionale Open Access dell'Università di Torino

Pressure-induced water intrusion in FER-type zeolites and the influence of extraframework species on structural deformations

This is the author's manuscript

Original Citation:

Availability:

This version is available http://hdl.handle.net/2318/144313 since 2016-07-19T09:59:20Z

Published version:

DOI:10.1016/j.micromeso.2014.02.036

Terms of use:

Open Access

Anyone can freely access the full text of works made available as "Open Access". Works made available under a Creative Commons license can be used according to the terms and conditions of said license. Use of all other works requires consent of the right holder (author or publisher) if not exempted from copyright protection by the applicable law.

(Article begins on next page)

16 October 2026

Elsevier Editorial System(tm) for
Microporous & Mesoporous Materials
Manuscript Draft

Manuscript Number: MICMAT-D-14-00037R3

Title: Pressure-induced water intrusion in FER-type zeolites and the influence of extraframework species on structural deformations

Article Type: Full Length Article

Keywords: Ferrierite; High-Pressure; Synchrotron X-Ray Powder Diffraction; water intrusion.

Corresponding Author: Dr. Rossella Arletti,

Corresponding Author's Institution: University of Turin

First Author: Rossella Arletti

Order of Authors: Rossella Arletti; Giovanna Vezzalini; Simona Quartieri; Francesco Di Renzo; Vladimir Dmitriev

Abstract: The response to pressure of a natural ferrierite from Monastir (Sardinia, Italy) (Mon-FER) and of the synthetic all-silica phase (Si-FER) was investigated by means of in-situ synchrotron X-ray powder diffraction in the presence of penetrating (methanol:ethanol:water 16:3:1, m.e.w.) and non-penetrating (silicone oil, s.o.) pressure transmitting media (PTM). The following aspects are discussed: i) the penetration of extra-water molecules into the all-silica phase and the related structural aspects involving both framework and extraframework systems; ii) the influence of the zeolite composition and of the different PTM used in the compression experiments on the overall elastic parameters of the two investigated samples; iii) the elastic parameters and the unit cell P-induced deformations of the mineral phase; iv) the reversibility extents of the observed phenomena. Evidence of water penetration during compression of Si-FER in m.e.w. was found. The refinement performed at 0.2 GPa enabled location of 15 water molecules forming bulk-like and monodimensional water clusters. No methanol or ethanol penetration was observed. The results demonstrate that the free volume of the porous material is not the only parameter influencing water condensation since applied pressure is an additional fundamental factor. The bulk modulus value calculated from Pamb to 4.9 GPa for Mon-FER (K0 =44 GPa, Kp=0.2) is intermediate between the lowest (about 14 GPa) and the highest (about 72 GPa) values determined to date for zeolites compressed in non-penetrating PTM. The highest P-induced deformations are observed for Si-FER compressed in s.o. In general, higher rigidity for the natural sample was found in both media.

UNIVERSITA' DEGLI STUDI DI TORINO

Dipartimento di Scienze della Terra

Torino, February 21th 2013

Dear Editor,

please find enclosed the revised version of manuscript **PRESSURE-INDUCED WATER INTRUSION IN FER-TYPE ZEOLITES AND THE INFLUENCE OF EXTRAFRAMEWORK SPECIES ON STRUCTURAL DEFORMATIONS** by Rossella Arletti, Giovanna Vezzalini, Simona Quartieri, Vladimir Dmitriev and Francesco Di Renzo.

All the reviewers requests were fulfilled: the references were corrected and the keywords were added after the abstract.

We hope that now our paper will be suitable for publication.

Best regard

Rossella Arletti

Highlights

- Penetration of 15 water molecules in synthetic Si-FER compressed in m.e.w was found.
- Eleven water molecules in the 10MR channels, forming bulk-like clusters.
- Four molecules were located in the FER cage as monodimensional clusters.
- Natural FER shows higher rigidity in m.e.w. and s.o. respect to the synthetic one.
- The presence of extraframework species in natural FER stiffens the structure.

***Graphical Abstract (for review)**

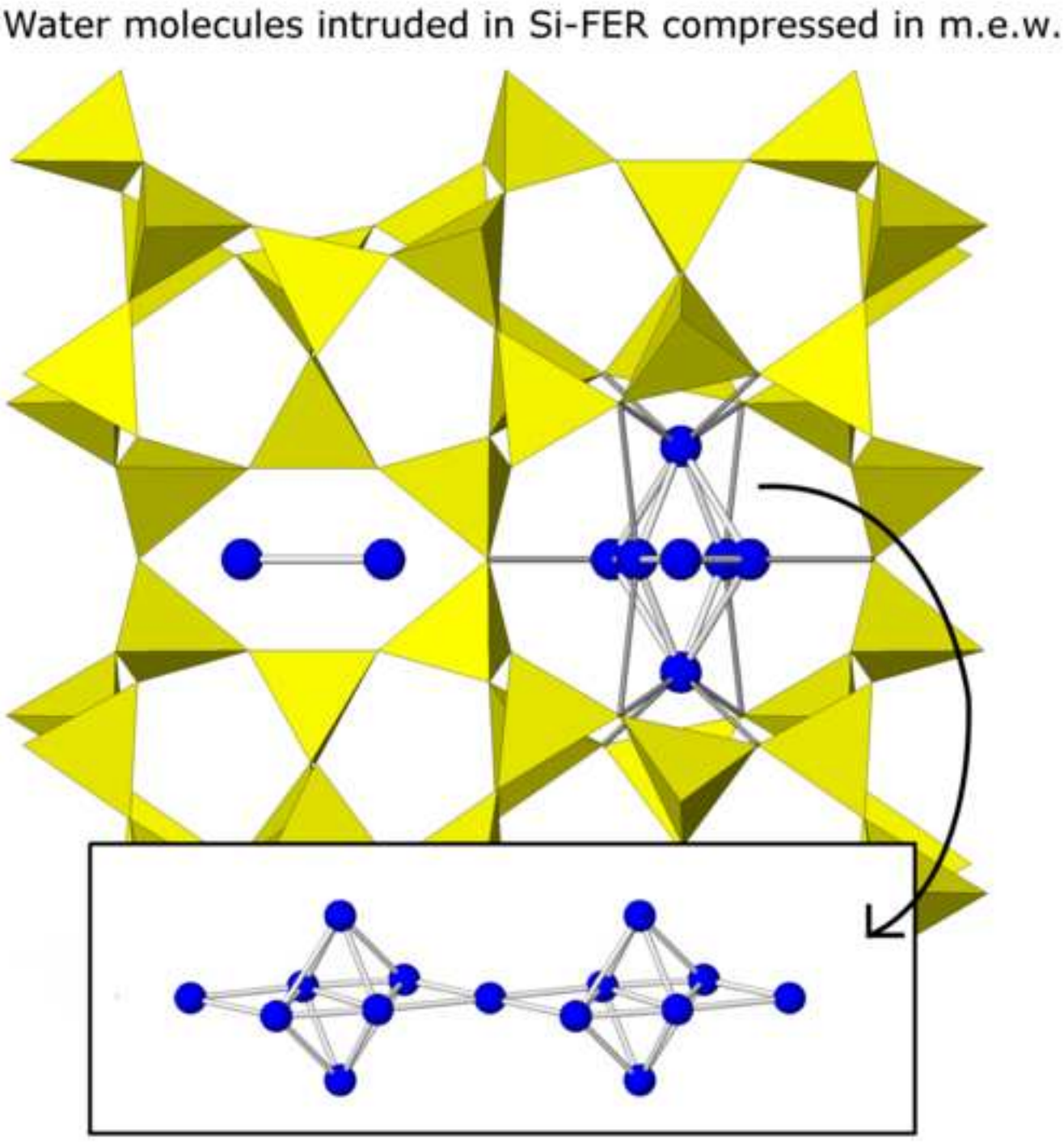

*Manuscript
Click here to download Manuscript: manuscript_rev-BIBLIO.docx Click here to view linked References

Pressure-induced water intrusion in FER-type zeolites and the influence of extraframework species on structural deformations

Rossella Arletti[1]*, Giovanna Vezzalini[2], Simona Quartieri[3], Francesco Di Renzo[4], Vladimir Dmitriev[5]

[1]*Dipartimento di Scienze della Terra, Università di Torino*

Via Valperga Caluso 35, Torino, Italy.

[2]*Dipartimento di Scienze Chimiche e Geologiche, Università di Modena e Reggio Emilia,*

Via S. Eufemia 19, 41100 Modena, Italy.

[3]*Dipartimento di Fisica e Scienze della Terra , Università di Messina,*

Viale Ferdinando Stagno d'Alcontres 31, 98166 Messina S. Agata, Italy.

[4]*Institut Charles Gerhardt Montpellier, ENSCM*

8 Rue Ecole Normale, F-34296 Montpellier

[5]*Swiss–Norwegian Beam Line at ESRF, BP220, 38043 Grenoble Cedex, France*

**rossella.arletti@unito.it*

Abstract

The response to pressure of a natural ferrierite from Monastir (Sardinia, Italy) (Mon-**FER**) and of the synthetic all-silica phase (Si-**FER**) was investigated by means of in-situ synchrotron X-ray powder diffraction in the presence of penetrating (methanol:ethanol:water 16:3:1, m.e.w.) and non-penetrating (silicone oil, s.o.) pressure transmitting media (PTM). The following aspects are discussed: *i)* the penetration of extra-H_2O molecules into the all-silica phase and the related structural aspects involving both framework and extraframework systems; *ii)* the influence of the

zeolite composition and of the different PTM used in the compression experiments on the overall elastic parameters of the two investigated samples; *iii)* the elastic parameters and the unit cell P-induced deformations of the mineral phase; *iv)* the reversibility extents of the observed phenomena. Evidence of H_2O molecules penetration during compression of Si-**FER** in m.e.w. was found. The refinement performed at 0.2 GPa enabled location of 15 H_2O molecules forming bulk-like and monodimensional H_2O clusters. No methanol or ethanol penetration was observed. The results demonstrate that the free volume of the porous material is not the only parameter influencing water condensation since applied pressure is an additional fundamental factor. The bulk modulus value calculated from P_{amb} to 4.9 GPa for Mon-**FER** (K_0 =44 GPa, Kp=0.2) is intermediate between the lowest (about 14 GPa) and the highest (about 72 GPa) values determined to date for zeolites compressed in non-penetrating PTM. The highest P-induced deformations are observed for Si-**FER** compressed in s.o. In general, higher rigidity for the natural sample was found in both media.

Keywords: Ferrierite, High-Pressure, Synchrotron X-Ray Powder Diffraction, water intrusion.

INTRODUCTION

Ferrierite (framework type **FER**,[1]) is both a well-known zeolite mineral [2,3] and a synthetic porous material, prepared readily by both aqueous [4] and non-aqueous routes [5]. Its crystal structure [6-8] (Figure 1a,b) is built up of rings of five SiO_4 tetrahedra (known as 5MR building units), which form layers on the *ab* plane. The layers are connected to form 10MR channels running parallel to [001], which are intersected by 8MR channels running parallel to the [010]. Six-membered rings connect the 10MRs channels along [010]. The structure contains cavities known as **FER** cages, formed by the intersection of the eight-membered ring channels and the six-membered ring channels (parallel to the *c*-axis).

An understanding of the stability and properties of ferrierite is of interest, beyond the mineralogical implications, because of the role of this porous material in many industrial processes.

For example, it is used in the petrochemical industry as a shape selective catalyst for the production of isobutene [9]. In its Si-rich form, ferrierite has also been used for water purification [10,11].

Ferrierite has been studied at high temperature (HT) by [12], working on the high silica form, while its high pressure (HP) behavior has never been investigated until now. In addition to HT, HP can also induce important structural changes in zeolites, modifying their physical and chemical properties and, consequently, their possible applications [13,14]. It is well known that HP studies on porous materials can be performed using either penetrating or non-penetrating pressure-transmitting media (PTM). The former are usually aqueous/alcohol mixtures, with molecular sizes small enough to penetrate the zeolite porosities (see for example [15] and [16] for a review); the latter are usually silicone oil or glycerol, with molecules too large to penetrate the zeolite (see e.g. [14, 17-24]). While non-penetrating PTM are mainly used to study zeolite compressibility, P-induced phase transitions, and amorphization, the penetrating ones can be usefully exploited for investigating the so-called pressure induced hydration (PIH) effect [25], which consists in the penetration of additional H_2O molecules into the zeolite channels. This phenomenon - which usually occurs from ambient conditions to about 3 GPa [16] - is particularly interesting in the case of irreversibility of the process upon P release, since, in this case, a new material of different composition and possibly different properties is produced. Moreover, understanding the changes in water structure as a consequence of the interactions with confining surfaces is of paramount interest for several technological applications (i.e. inhibition of corrosion, heterogeneous catalysis, design of super-hydrophobic surfaces, biological membranes, water purification) [26]. The interest in the confinement of water in nanoscopic spaces, like zeolitic cavities, stems from the fact that the properties of confined water are believed to be very different from those of the bulk fluid. Finally, it has been shown that the intrusion of extra-guest species into zeolite cavities also has important consequences on the overall elastic behavior of the material, since the new guest molecules generally contribute to stiffening the structure and countering P-induced deformations [18,23,24,27-29].

In addition to PIH - occurring under pressure values of the order of GPa - another phenomenon has attracted renewed interest in recent years: water condensation in hydrophobic all-silica zeolites, a process that occurs within the pressure regime of the MPa [see e.g. 30-33]. In general, different behaviors can be observed, depending on various physical parameters of the matrix, such as pore size, pore system, channel dimensionality (one-, bi- or three-dimensional) [34-37], and on the hydrophobic/hydrophilic character of the zeolite [33,38]. According to the reversible or irreversible character of the intrusion–extrusion cycle, ‘‘water – Si-zeolite’’ systems are able to restore, absorb or dissipate mechanical energy. Consequently, molecular “spring”, “damper” or “shock-absorber” behavior can be observed [36,37,39-42]. It must be noted, however, that none of these studies provided detailed structural information on ‘‘water – Si-zeolite’’ systems.

In this work the responses of two ferrierite samples to pressure in the presence of penetrating and non-penetrating PTM were studied: natural ferrierite from Monastir (Sardinia, Italy) (hereafter Mon-**FER**), and the synthetic all-silica phase (hereafter Si-**FER**). The following aspects will be discussed:

i) the penetration of extra-H_2O molecules into the all-silica phase and the related structural aspects involving both framework and extraframework systems;
ii) the influence of the zeolite composition and of the different PTM used in the compression experiments on the overall elastic behavior of the two investigated samples;
iii) the elastic parameters and the unit cell P-induced deformations of the mineral phase;
iv) the reversibility extents of the observed phenomena.

EXPERIMENTAL METHODS AND DATA ANALYSIS

Mon-**FER** was chemically and physically characterized by Orlandi and Sabelli, [43] and by Alberti and Sabelli [7]. Its chemical formula is $(Na_{0.56}K_{1.19}Mg_{2.02}Ca_{0.52}Sr_{0.14})(Al_{6.89}Si_{29.04})O_{72} \cdot 17.86\ H_2O$.

The synthetic Si-**FER** was synthesized following the synthesis procedure reported in [44].The synthesized Si-Fer was heat-treated for 72 h at 850 °C to remove the templates. The chemical composition was determined using a Cameca SX 50 electron microprobe on a pellet of the zeolite powder (experimental conditions: 20 kV, beam current 2 nA, the standards used were natural minerals). The resulting chemical formula was [$Si_{36}O_{72}$]. Thermo-gravimetric analysis was performed in air on 9.62 mg of sample, using a Seiko SSC/5200 instrument, operating at 10 °C/min heating rate, from RT to 900 °C. The weight loss (< 0.5 wt %) testified that all the organic compounds used as template agents [i.e. pyridine (C_5H_5N) and propylamine –(*n*-C_3H_9N)] were eliminated from the channels.

XRPD experiments at ambient pressure

X-Ray Powder Diffraction (XRPD) experiments were performed at the SNBL1 (BM01a) beamline at ESRF. The diffraction data were collected in the Debye–Scherrer geometry on an image plate with a fixed wavelenght of 0.6973 Å. Data collections at ambient pressure (P_{amb}) were performed on powder samples placed in a 0.3 mm quartz capillary mounted on a goniometric spinning head. One-dimensional diffraction patterns of the two ferrierite samples (Figure 2a,b) were obtained by integrating the two dimensional images with the program FIT2D [45]. Rietveld profile fitting was performed in the 2θ range 3-35° using the GSAS package [46] with the EXPGUI [47] interface. The starting atomic coordinates were from the structural model of Alberti and Sabelli [7], and of Morris et al. [8] for natural and synthetic samples, respectively. The background curve was fitted by a Chebyshew polynomial with 20 coefficients. The pseudo-Voigt profile function proposed by [48] was applied, and the peak intensity cut-off was set to 0.1% of the peak maximum. Soft-restraints were applied to the T-O distances [Si-O = 1.58(2)-1.62(2)] and the weight was gradually decreased after the initial stages of refinement, up to a final weight equal to 10. The isotropic displacement parameters were constrained in the following way: the same value for all tetrahedral cations, a second value for all framework oxygen atoms, and a third one for the

extraframework species. The unit-cell parameters were allowed to vary for all refinement cycles. Details of the structural refinements are reported in Table 1.

XRPD experiments at high pressure

The H*P* experiments were carried out using modified Merril-Bassett DACs [49]. Two different experiments were performed on each sample, using two PTMs: methanol:ethanol:water 16:3:1 (m.e.w.), as penetrating PTM, and silicone oil (s.o.), as non-penetrating PTM. Pressure was calibrated using the ruby fluorescence method [50] on the non-linear hydrostatic pressure scale [51]. The estimated precision in the P values is 0.05 GPa [51]. The experiments were performed in the following P ranges: 1) for Mon-**FER**, from 0.1 to 7.3 GPa in the experiment in m.e.w. and from 0.4 to 8.3 GPa in s.o.; 2) Si-**FER**, from 0.1 to 8.1 GPa in the experiment in m.e.w. and from 0.2 to 8.2 GPa in s.o. Some patterns were also collected upon decompression from the highest pressure to P_{amb} for all the experiments. Selected integrated patterns from the four ramps are reported in Figure 3a,b,c, d.

Unit cell parameters of Mon-**FER** were determined by Rietveld profile fitting up to 7.0 and 5.7 GPa in m.e.w. and s.o., respectively, the data quality at higher pressure values being too low (i.e. too broad reflections with low intensities) for further refinements The synthetic sample underwent a phase transition from Pmnn to $P2_1/n$ s.g. at 1.8 GPa and 1.1 GPa when compressed in m.e.w. and s.o., respectively. Since the H*P* data quality was too low for structural refinements, the cell parameters were obtained with Le Bail method [52] from 1.8 to 7.1 GPa for the experiment in m.e.w. and only at 3.6 GPa for the ramp in s.o. In the latter case, the excessive broadening of the peaks in the range 1.1-3.6 GPa – probably due to the persistence of both orthorhombic and monoclinic phases – hindered cell refinement in this P range.

The quality of the powder data collected on Si-**FER** in m.e.w. allowed the structural refinement to converge successfully for the experiments at 0.2 GPa and upon decompression (P_{amb} (rev)). The initial atomic coordinates of these refinements were taken from the refinement at P_{amb}. The

integration data procedure and refinement strategy were the same as those employed for P_{amb} data analysis. Details of the data collection and of the structure refinements for Si-**FER** at P_{amb}, 0.2 GPa, (m.e.w.), P_{amb}(rev) (m.e.w.) are reported in Table 1. The refined cell parameters as a function of pressure for natural and synthetic ferrierite in m.e.w. and s.o. are reported in Table 2. Atomic coordinates, site occupancies and isotropic displacement parameters are reported in Table 3, and selected interatomic distances in Table 4.

RESULTS

Elastic behavior

Mon-**FER**

From Figure 3a,b - which shows selected powder patterns of Mon-**FER** compressed in m.e.w. and s.o., respectively - it is evident that the peak intensity ratios change upon *P* increase. Moreover, while for the sample compressed in m.e.w. the peak profiles remain sharp, a marked peak broadening is observed for the patterns collected in s.o. In both experiments, ferrierite does not undergo complete amorphization and, upon pressure release, the features characteristic of the low P patterns are reversibly regained.

When the sample is compressed in m.e.w. from P_{amb} to 7.0 GPa, a volume contraction of 12.2% is observed, while the unit cell parameters *a*, *b* and *c* decrease by 3.9, 3.8, and 5 %, respectively (Table 2 and Figure 5a). In the plot reporting the variation of cell parameters *vs.* pressure (Figure 5a), an increase in compressibility from about 1.8 GPa is observed. Finally, the unit cell parameters of the P_{amb} structure are well recovered upon decompression.

As previously discussed, Mon-**FER** was compressed in s.o. up to 8.3 GPa, but the unit cell parameters were successfully refined only up to 5.7 GPa, due to the low quality of the data at higher P values. In this P-range, *a*, *b*, *c*, and *V* reductions are: 3.6, 3.9, 3.6, and 10.8%, respectively (Table 2 and Figure 5b). In this case, the unit cell parameters are very well recovered upon pressure

release, with the exception of the pattern collected at 4.7 GPa, which corresponds to a slightly larger cell than expected, in particular along the *a* axis.

In this experiment, a change in compressibility is again observed during compression, but the compressibility decreases, as expected, at high P regime. The elastic behavior of Mon-**FER** compressed in s.o. is described by a third-order Birch-Murnaghan equation of state [53]. The bulk modulus, calculated in the P range P_{amb}-4.9 GPa using the data weighted by the uncertainties in P and V, is K_0 = 44(1) with K' = 0.2 (9) and V_0 = 2041(1).

Si-**FER**

The refinement of synthetic ferrierite at P_{amb} shows a structure perfectly consistent with that reported by Morris et al. [8]. An inspection of the electronic density maps established that the template agent was completely removed by calcination and no H_2O molecules were present in the porosities.

The selected powder patterns, collected during compression, reported in Figure 3c,d evidence P-induced changes in peak profiles and intensities in both m.e.w. and s.o. experiments. In particular, comparing the patterns of Figure 3c,d with that collected at P_{amb} (Figure 2b), a strong intensity decrease of the peaks at low 2ϑ angles is observed. Moreover, two very weak diffraction peaks arise at about 1.7 GPa, suggesting a phase transition to the monoclinic space group $P2_1/n$ (Figure 4).

From P_{amb} to 7.1 GPa, an overall unit cell volume reduction of about 15.2 % is observed for Si-**FER** compressed in m.e.w., while the unit cell axes undergo the following reductions: Δa = 6.5, Δb = 5.2, Δc = 4.3% (Table 2 and Figure 5a). As observed for the natural sample, a slope change is present in the *V vs. P* curve between 1 and 1.4 GPa. At this pressure the *a* parameter - which in the first compression regime is the most rigid axis - becomes the most compressible one (Figure 6a). Above 5 GPa, a slight decrease in compressibility is observed. Once the pressure is released, the structure regains its original orthorhombic symmetry and cell parameters.

The low quality of the data collected in s.o. and the associated peak broadening did not allow cell parameters refinements across the whole pressure range. After the phase transition occurring at about 1.6 GPa, only the pattern collected at 3.6 GPa allowed extraction of unit cell parameters, revealing a volume contraction of 14 %. This large *V* decrease essentially derives from the *a* parameter variation, while *b* and *c* remain almost constant. The same reversible behavior observed for Si- **FER** in m.e.w. is also found upon decompression in s.o.

Water intrusion in Si-FER

As previously reported, detailed structural data were only obtained for the Si-**FER** compressed in m.e.w. at 0.2 GPa and after pressure release at ambient conditions (P_{amb} (rev)) (Figures 7, 8 and Tables 3, 4). The refinement performed at 0.2 GPa enabled location of 15 H_2O molecules distributed in the channels in five independent crystallographic positions. No penetration of methanol and ethanol was observed, even though it was impossible to exclude the penetration of some alcohol molecules with a disordered distribution in a number of different positions. Eleven H_2O molecules were located by Fourier difference maps in the 10MR channel. Three fully occupied H_2O sites (W1, W2, and W5 in Figure 7) form a chain on the mirror plane perpendicular to the *a* axis (Figure 9). Another partially occupied (30%) W4 site lies outside the mirror plane, coordinating four framework oxygen atoms and four H_2O molecules (W2 and W5 in Table 4) sited on the mirror plane (Figures 7 and 9). Likewise, W2 and W5 coordinate both framework oxygen atoms and H_2O molecules, while W1 is bonded only to H_2O molecules. In addition, dumbbells of W3 H_2O molecules - accounting for four molecules in the unit cell - were located at the intersection in the **FER** cage (Figure 7).

The compression exerted by the PTM, along with the penetration of H_2O molecules inside the zeolite cavities - and the consequent establishment of hydrogen bonds with the framework oxygen atoms - induce deformations in the Si-**FER** framework. In particular, the strongest deformation is observed at the 6MR, which becomes more elliptical (the O3-O3 distance decreases

from 4.83 to 4.28 Å, see Figure 7). Variations are also observed at the 10MR which, on the contrary, becomes more circular (O5-O5 x O9-O10= 8.13 x 7.34 at P_{amb} and 7.42 x 7.04 at 0.2 GPa, see Figure 7). This change is a consequence of the formation of the hydrogen bond W5 ···· O5 that contributes to stiffening the channel along [010]. Conversely, the formation of W4····O9 and W4····O10 bonds influences to a lesser extent the deformation of the channel, the W4 site being only partially occupied.

The refinement of the pattern collected upon decompression to ambient conditions shows the presence of 15.3 H_2O molecules, contrasting with the completely anhydrous Si-**FER**. Since it was impossible to refine the structure at the highest investigated pressures, there is no information on the maximum water loading achieved. However, it is definitely clear that the intrusion phenomenon is not completely reversible, even though the degree of reversibility is uncertain.

The excess H_2O molecules found in the P_{amb}(rev) refinement compared to that at 0.2 GPa is due to the presence of an additional partially occupied (15%) H_2O site (W6) compared to the 0.2 GPa refinement. This new site - located in the **FER** cage - gives rise to a zigzag chain, formed by W6 and two consecutive W3 molecules (Figures 8 and 10). Since the W6 site is empty at 0.2 GPa, this means that it is involved in water penetration at a higher pressure regime, where no structural refinements were performed. As a consequence, neither the final occupancy of this site can be defined, nor the reversibility degree of water penetration. Anyway, on the basis of the coordination distances with the framework, we can suppose that this site can host a remarkable amount of H_2O molecules. The existence of other H_2O sites filled at higher pressure and subsequently emptied upon decompression cannot be excluded.

The H_2O sites occupying the 10MR channel remain more or less in the same positions found at 0.2 GPa, with only W2 losing its bond interaction with the framework oxygen O9, but maintaining its coordination with the other H_2O molecules (Table 4 and Figure 8).

DISCUSSION

Comparison between Mon*-FER *and Si*-FER *compressibility

Both experiments on Mon-**FER** reveal rather isotropic unit cell parameter variations upon compression. This is particularly evident in the experiment with s.o., while in m.e.w. a slightly higher contraction of the *c* parameter is observed above 1.8 GPa. Moreover, below this pressure value, compressibility in m.e.w. is lower than in the higher P regime. This can be ascribed to the entrance of some PTM molecules into the zeolite channels in the early stages of compression. This penetration is accompanied by a stiffening effect on the whole structure and by lower compression efficiency exerted by the medium, resulting in low compressibility. In s.o. this effect is prevented by the excessively large size of the PTM, and above 5 GPa the compressibility tends to decrease. The K_0 value (44 GPa, Kp=0.2) calculated from P_{amb} to 4.9 GPa is intermediate between the lowest (about 14 GPa) and the highest (about 72 GPa) values determined to date for zeolites compressed in "non-penetrating" P-transmitting media [20].

As previously reported, a marked decrease in intensity of the diffraction peaks at low 2θ is induced in Si-**FER** by compression in m.e.w. at about 0.2 GPa (Figures 2b and 3c). Above this pressure value, no further evident decreases are observed. Since the low-2θ angle peaks are strongly influenced by both the amount and the distribution of the extra-framework species, these intensity variations can be ascribed to the penetration of PTM molecules and the consequent increase in the extraframework content.

Concerning the elastic behavior of Si-**FER**, it is observed that the *a* cell parameter is more compressible than the other axes in both media. This is compatible with the presence, along the *b* and *c* axes, of pentasil chains, which are known to exhibit low deformability. Moreover, the analysis of the *P*-dependence of Si-**FER** unit cell parameters in s.o. reveals a dramatic deformation (ΔV = 14% at 3.6 GPa). This is interpreted as a consequence of the complete lack of extraframework species in this phase and the non-penetrability of s.o. molecules. At the same time, the higher rigidity of Mon-**FER** in both media and of Si-**FER** in m.e.w. can be explained by the

presence of extraframework species in the former and by the penetration of the PTM molecules in the latter, which both contribute to stiffening the structure.

Water confinement and condensation in hydrophobic zeolites

An important result of this work regards the evidence of water penetration and confinement during compression of Si-**FER** in m.e.w. In particular, the phenomenon is observed at 0.2 GPa in both 10MR channels and **FER** cage. Clusters formed by two W2 and two W5 molecules - connected through W1 to form planar aggregates - are systematically present in the 10MR channels. In 30% of the unit cells, the additional presence of a W4 molecule transforms these clusters into tridimensional aggregates (Table 4 and Figure 9), located at the intersection of the 10MR and the 8MR channels. Due to the lack of detailed structural data at higher pressure values, it cannot be excluded that the W4 occupancy factor might reach 100%, with the consequent presence of these clusters in all the unit cells in the HP regime. Concerning the **FER** cage, a small cluster of two W3 H_2O molecules is found at 0.2 GPa, while in the P_{amb}(rev) structure this cluster dimension increases to three molecules, due to the presence of the additional H_2O site W6. It is reasonable to argue that this W6 molecule persists upon decompression after the formation of the 3-molecule cluster at high pressure.

Similar HP-induced H_2O molecules clustering is also demonstrated for silicalite-1 in a simulation study [32] and justified by the 3D geometry of the pore intersections, which enables H_2O molecules to pile up in more or less the same way as in the bulk liquid. Bushuev and co-workers [54] - studying the water intrusion/extrusion phenomenon in hydrophobic pure silica zeolites through molecular dynamics simulations – report that “bulk-like” clusters form in microporous phases characterized by 12MR channels, while the presence of 10MR channels promotes the formation of chain-like clusters. The results of the present study on Si-**FER** demonstrate that bulk-like H_2O molecules clusters can also be formed in 10MR channels and that the free volume of the

zeosils is not the only parameter to influence water condensation, with applied pressure representing an additional fundamental factor.

In Si-chabazite, Trzpit and co-authors [38] found - through water intrusion/extrusion isotherms, ^{29}Si and ^{1}H NMR and X-ray powder diffraction - that H_2O molecules are trapped in the chabazite supercage. Two situations were identified: *i*) aggregates formed by molecules strongly hydrogen bonded with the framework silanols (formed upon intrusion-extrusion) and; *ii)* liquid-like physisorbed molecules, only interacting with other H_2O molecules.

Similar configurations were also observed in the Si-**FER** of the present study. In the 10MR channels, W2, W4, and W5 molecules are hydrogen-bonded to the framework, while W1 is bonded only to H_2O molecules. In the **FER** cage, the two W3 molecules found at 0.2 GPa are reciprocally bonded, while the additional W6 molecule found in the P_{amb}(rev) structure is strongly bonded to a framework oxygen atom (Table 4 and Figure 9).

Water intrusion in ferrierite was specifically investigated by Cailliez et al. (2008) [30] through mercury porosimetry and molecular simulations. These authors found that in ferrierite the process starts at 0.1 and 0.2 GPa, based on experimental and simulation data, respectively. Both the intrusion pressure and the total amount of H_2O molecules trapped in the silica ferrierite (about 15 molecules) are in close agreement with the structural results of the study, the main difference being related to the reversibility of the process. Cailliez et al. [30] found that the intrusion/extrusion phenomenon was reversible, within experimental uncertainties, while this was not confirmed in the present study. However, this discrepancy can be explained by the very marked compression (7.1 GPa) of the Si-**FER** in the latter. Under these conditions the formation of structural defects (silanols) and strong hydrogen bonds between H_2O molecules and framework oxygen atoms is encouraged, with consequent incomplete reversibility of the process.

In the same paper Cailliez et al. [30] compare the water intrusion/extrusion phenomenon observed in ferrierite and silicalite-1. They report that in silicalite-1 the intrusion is steeper and occurs at a lower pressure than in ferrierite, justifying this behavior with the smaller pore radii and

the consequent higher fluid confinement of water in ferrierite. An analogous comparison based on structural results is impossible, due to the lack of structural data on the HP-behavior of silicalite in m.e.w. The only data available in literature regard Na-[23] and H-ZSM5 [24].

In these hydrophilic zeolites – where the porosities are already occupied by H_2O molecules and extraframework cations at P_{amb} – the penetration of an additional 12 and 14 H_2O molecules is observed in H and Na-ZSM5, respectively, with the main intrusion occurring at about 0.8 GPa. This pressure is definitely higher than that generally found for hydrophobic porous materials [53]. Notwithstanding the fact that the intrusion pressure is expected to be lower for hydrophilic phases, this result can be explained by the need for the additional intruded H_2O molecules to shift the already present extraframework species and to occupy both new and already existing partially occupied sites in the channels.

ACKNOWLEDGEMENTS

The BM01 beamline at the European Synchrotron Radiation Facility is acknowledged for allocation of experimental beamtime. This work was supported by the Italian MIUR, within the framework of the following projects: PRIN2009 “Struttura, microstruttura e proprietà dei minerali”; PRIN2010-11 “Dalle materie prime del sistema Terra alle applicazioni tecnologiche: studi cristallochimici e strutturali”; FIRB, Futuro in Ricerca “Impose Pressure and Change Technology” (RBFR12CLQD).

[1] Ch. Baerlocher, L.B. McCusker, D.H. Olson, Atlas of Zeolite Framework Types, sixth ed., Elsevier, Amsterdam, 2007.

[2] G. Gottardi and E. Galli, Natural Zeolites, Springer-Verlag, Berlin, 1985.

[3] W.S. Wise, R.W Tschernich, Am. Mineral. 61 (1976) 60 - 66

[4] H. Gies, R.P. Gunawardane, Zeolites 7 (1987) 442 - 445

[5] A. Kuperman, S. Nadimi, S. Oliver, G.A. Ozin, J.M., Garces, M.M. Olken, Nature 365 (1993) 239 - 242

[6] P.A. Vaughan, Acta Crystallogr., 21 (1966) 983-990

[7] A. Alberti, C. Sabelli, Z. Kristallogr. 178 (1987) 249- 256

[8] R.E. Morris, S.J. Weigel, N.J. Henson, L.M. Bull, M.T. Janicke, B.F. Chmelka, A.K. Cheetham, J. Am. Chem. Soc. 116 (1994) 11849-11855

[9] K. Yamahara, K. Okazaki, K. Kawanura, Catal. Today 23 (1995) 397- 402

[10] R. N. Eissmann, M. D. LeVan, Ind. Eng. Chem. Res. 32 (1993) 2752-2757.

[11] J. Stelzer, M. Paulus, M. Hunger, J. Weitkamp, Microporous Mesoporous Mater. 22 (1998) 1-8.

[12] I. Bull, P. Lightfoot, L.A. Villaescusa, L.M. Bull, R.K.B. Gover, J.S.O. Evans, R.E. Morris J. Am. Chem. Soc. 125 (2003) 4342-4349.

[13] R. Arletti, O. Ferro, S. Quartieri, A. Sani, G. Tabacchi, G. Vezzalini, Am. Mineral. 88 (2003) 1416-1422

[14] G.D. Gatta, Z. Kristallogr. 223 (2008)160-170.

[15] C. Betti, E. Fois, E. Mazzucato, C. Medici, S. Quartieri, G. Tabacchi, G. Vezzalini, V. Dmitriev, Microporous Mesoporous Mater. 103 (2007) 190–209.

[16] S. Ori, S. Quartieri, G. Vezzalini, V. Dmitriev, Am. Mineral. 93 (2008) 1393-1403.

[17] R. Arletti, S. Quartieri, G. Vezzalini, Am. Mineral. 95 (2010) 1247-1256.

[18] R. Arletti, G. Vezzalini, A. Morsli, F. Di Renzo, V. Dmitriev, S. Quartieri, Microporous Mesoporous Mater. 142 (2011) 697–707.

[19] E. S. Fois, A. Gamba, C. Medici, G. Tabacchi, S. Quartieri, E. Mazzucato, R. Arletti, G. Vezzalini, V. Dmitriev, Microporous Mesoporous Mater. 115 (2008) 267-280.

[20] L. Leardini, S. Quartieri, G. Vezzalini, Microporous Mesoporous Mater. 127 (2010) 219–227.

[21] L. Leardini, S. Quartieri, A. Martucci, G. Vezzalini, V. Dmitriev, Z. Kristallogr. 227 (2012) 514-521.

[22] L. Leardini, S. Quartieri, G. Vezzalini, A. Martucci, V. Dmitriev, Microporous Mesoporous Mater. 170 (2013) 52–61.

[23] S. Quartieri, G. Montagna, R. Arletti, G. Vezzalini, J. Solid State Chem. 184 (2011) 1505–1516.

[24] S. Quartieri, R. Arletti, G. Vezzalini, F. Di Renzo, V. Dmitriev, J. Solid State Chem. 191 (2012) 201–212.

[25] Y. Lee, J.A., Hriljac, A. Studer, T. Vogt, Phys. Chem. Mineral. 31 (2004) 22-27.

[26] N. Giovambattista, P.J. Rossky, P.G. Debenedetti, Phys. Rev. E, 73 (2006) 041604-14

[27] E. Fois, A. Gamba, G. Tabacchi, R. Arletti, S. Quartieri, G. Vezzalini, Am. Mineral. 90 (2005) 28–35.

[28] E. Fois, A. Gamba, G. Tabacchi, S. Quartieri, R. Arletti, G. Vezzalini, in: A. Gamba, C. Colella, S. Coluccia (Eds.), Stud. Surf. Sci. Catal., vol. 155, Elsevier, Amsterdam, 2005, pp. 271–280.

[29] G.D.Gatta, Eur. J. Mineral. 17 (2005) 411-422.

[30] F. Cailliez, M. Trzpit, M. Soulard, I. Demachy, A. Boutin, J. Patarin, A.H. Fuchs, Phys. Chem. Chem. Phys. 10 (2008) 4817–4826.

[31] P. Demontis, G. Stara, G.B. Suffritti, J. Phys. Chem. B 107 (2003) 4426-4436.

[32] N. Desbiens, I. Demachy, A.H. Fuchs, H. Kirsch-Rodeschini, M. Soulard, J.Patarin, Angew. Chem. Int. Ed. 44 (2005) 5310 –5313.

[33] M. Trzpit, M. Soulard, J. Patarin , N. Desbiens, F. Cailliez, A. Boutin, I. Demachy , A.H. Fuchs, Langmuir 23 (2007) 10131-10139.

[34] A. Y. Fadeev, V.A. Eroshenko, J. Colloid Interface Sci. 187 (1997) 275-282.

[35] T. Martin, B. Lefevre, D. Brunel, A. Galarneau, F. Di Renzo, F. Fajula, P.F. Gobin, J.F. Quinson, G. Vigier, Chem. Commun. 2002 (2002) 24-25.

[36] M. Trzpit, M. Soulard, J. Patarin, Mater. Sci. 44 (2009) 6525–6530.

[37] M. Trzpit, M. Soulard, J. Patarin, Microporous Mesoporous Mater. 117 (2009) 627-634.

[38] M. Trzpit, S. Rigolet, J.L. Paillaud, C. Marichal, M. Soulard, J. Patarin, J. Phys. Chem. B 112 (2008) 7257-7266.

[39] Cailliez, A. Boutin, I. Demachy , A.H. Fuchs, Mol. Simul. 35 (2009) 24-30.

[40] V. Eroshenko, R.C. Regis, M. Soulard, J. Patarin, J. Am. Chem. Soc. 123, (2001) 8129-8130.

[41] V. Eroshenko, R.C. Regis, M. Soulard, J. Patarin, C. R. Physique 3 (2002) 111-119.

[42] M. Soulard, J. Patarin, V. Eroshenko, R.C. Regis, Proc. 14th, Int. Zeolite Conf. (2004) 1830.

[43] P. Orlandi, C. Sabelli N. Jb. Mineral.. Mh. 1983 (1983) 498 - 504.

[44] R. A. Rakoczy, Y. Traa, P. Kortunov, S. Vasenkov, J. Kärger, J. Weitkamp, Microporous Mesoporous Mater. 104 (2007) 179–184.

[45] A.P. Hammersley, S.O. Svensson, M. Hanfland, A.N. Fitch, D. Häusermann, High Pressure Res. 14 (1996) 235–248.

[46] A.C. Larson, R.B. Von Dreele, GSAS-General Structure Analysis System, Report LAUR 86-748, Los Alamos National Laboratory, Los Alamos, New Mexico, 1996.

[47] B.H. Toby, J. Appl. Crystallogr. 34 (2001) 210–213.

[48] P. Thomson, D.E. Cox, J.B. Hastings, J. Appl. Crystallogr. 20 (1987) 79–83.

[49] R. Miletich, D.R. Allan, W.F. Kush, in: R.M. Hazen, R.T. Downs (Eds.), High- Temperature and High-Pressure Crystal Chemistry, Reviews in Mineralogy and Geochemistry, vol. 41, Mineralogical Society of America and Geochemical Society, Washington, USA, 2000, pp. 445–519.

[50] R.A. Forman, G.J. Piermarini, J.D. Barnett, S. Block, Science 176 (1972) 4673–4676.

[51] H.K. Mao, J. Xu, P.M. Bell, J. Geophys. Res. 91 (1986) 4673–4676.

[52] A. Le Bail, H. Duroy, J.L. Fourquet, Mater. Res. Bull. 23 (1988) 447–452.

[53] F. Birch, Phys. Rev. 71 (1947) 809–824.

[54]Y. G. Bushuev, G. Sastre, G.V. de Julián-Ortiz, J. Gálvez, Journal of Physical Chemistry C, 116 (2012) 24916-24929.

Figure1a

Click here to download high resolution image

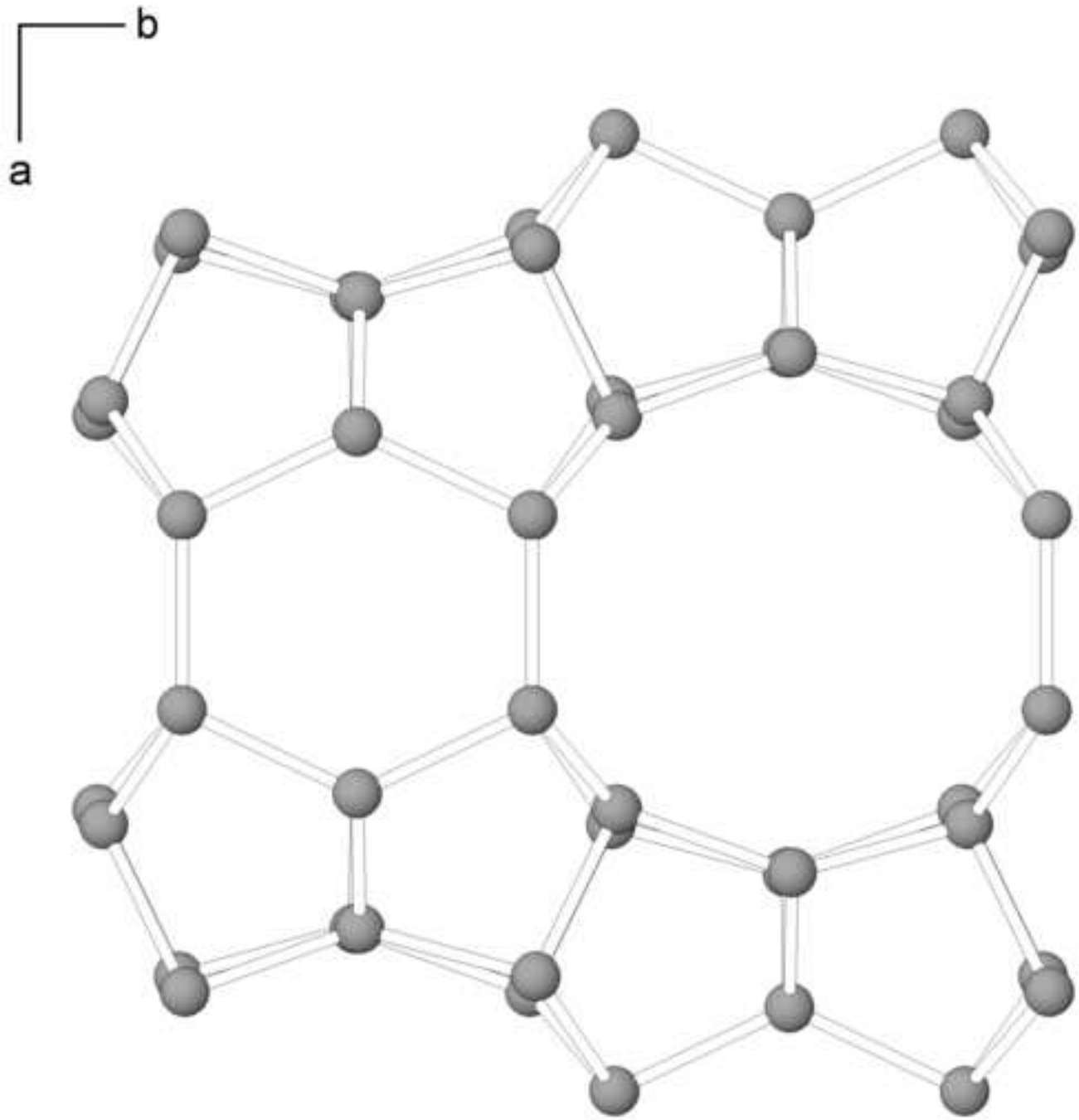

Figure1b
Click here to download high resolution image

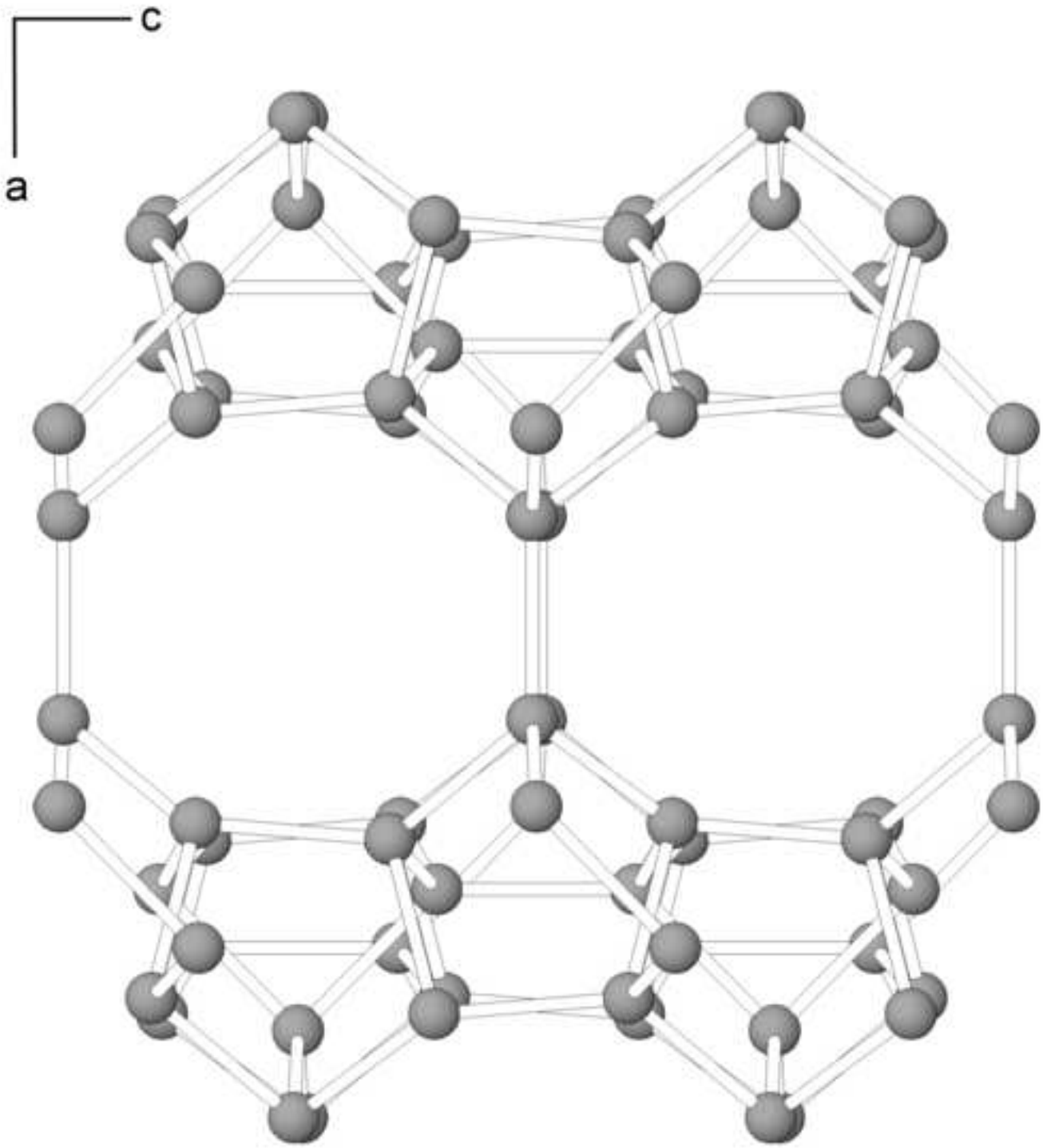

Figure4

Click here to download high resolution image

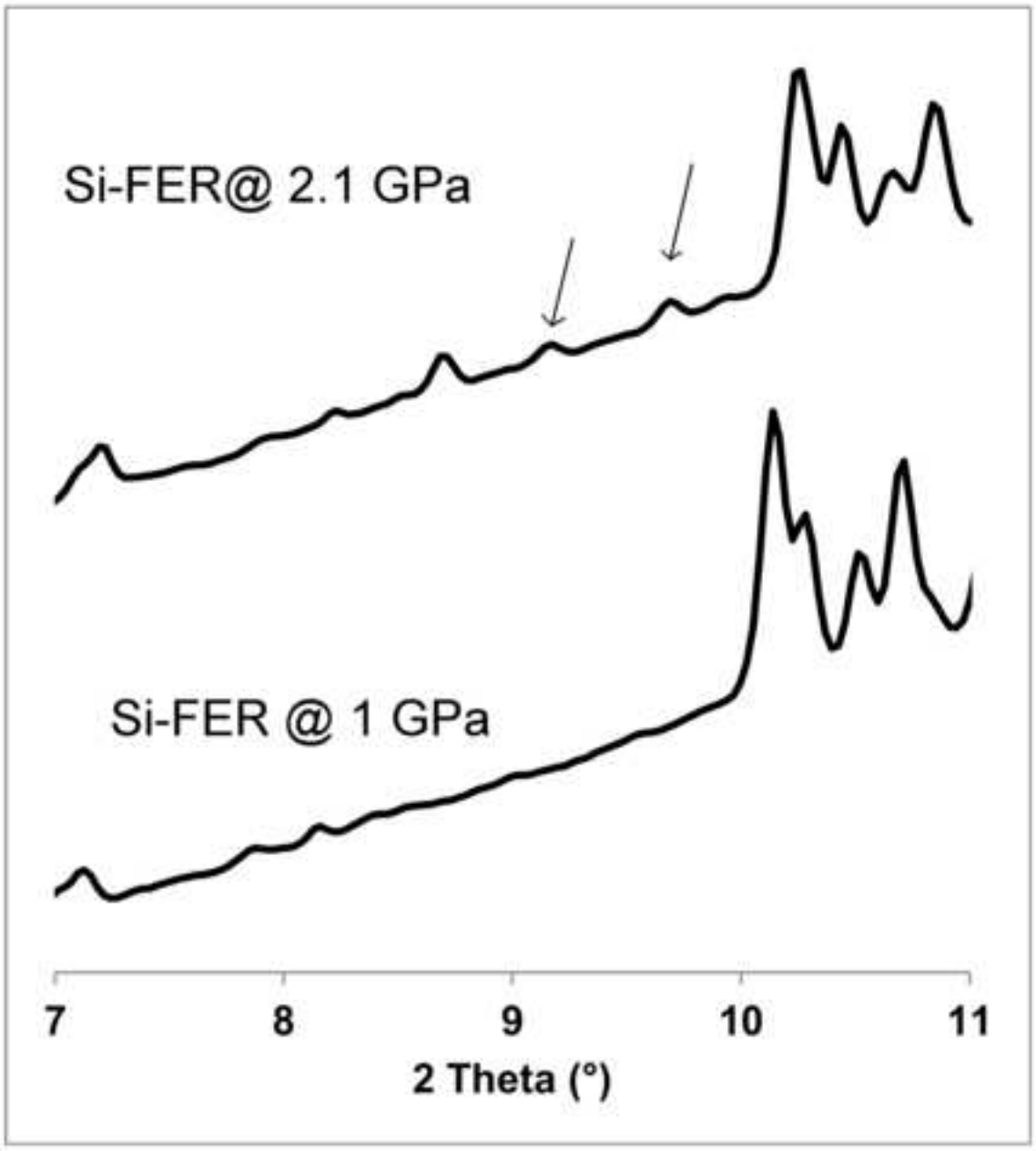

Figure5a

Click here to download high resolution image

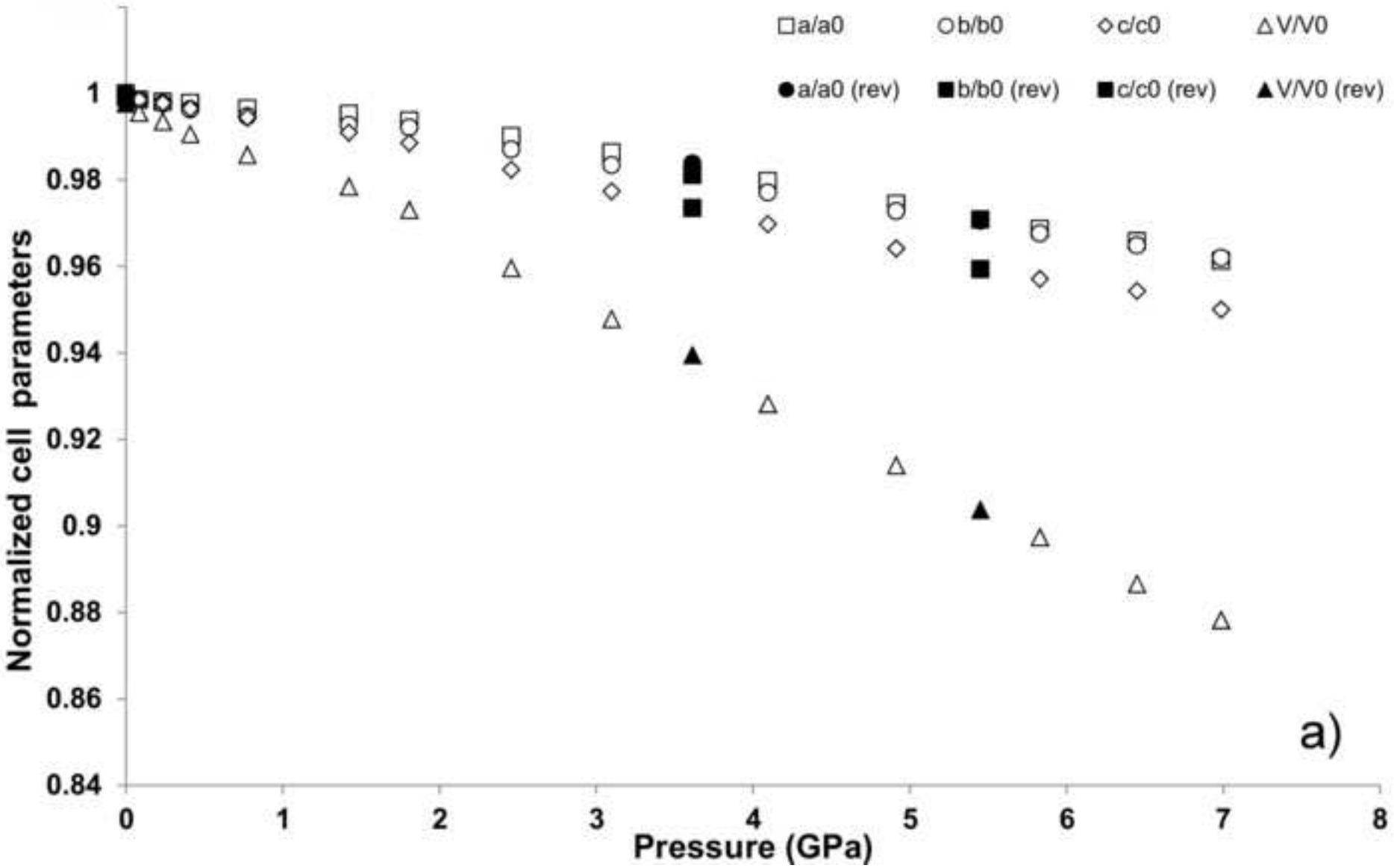

Figure5b

Click here to download high resolution image

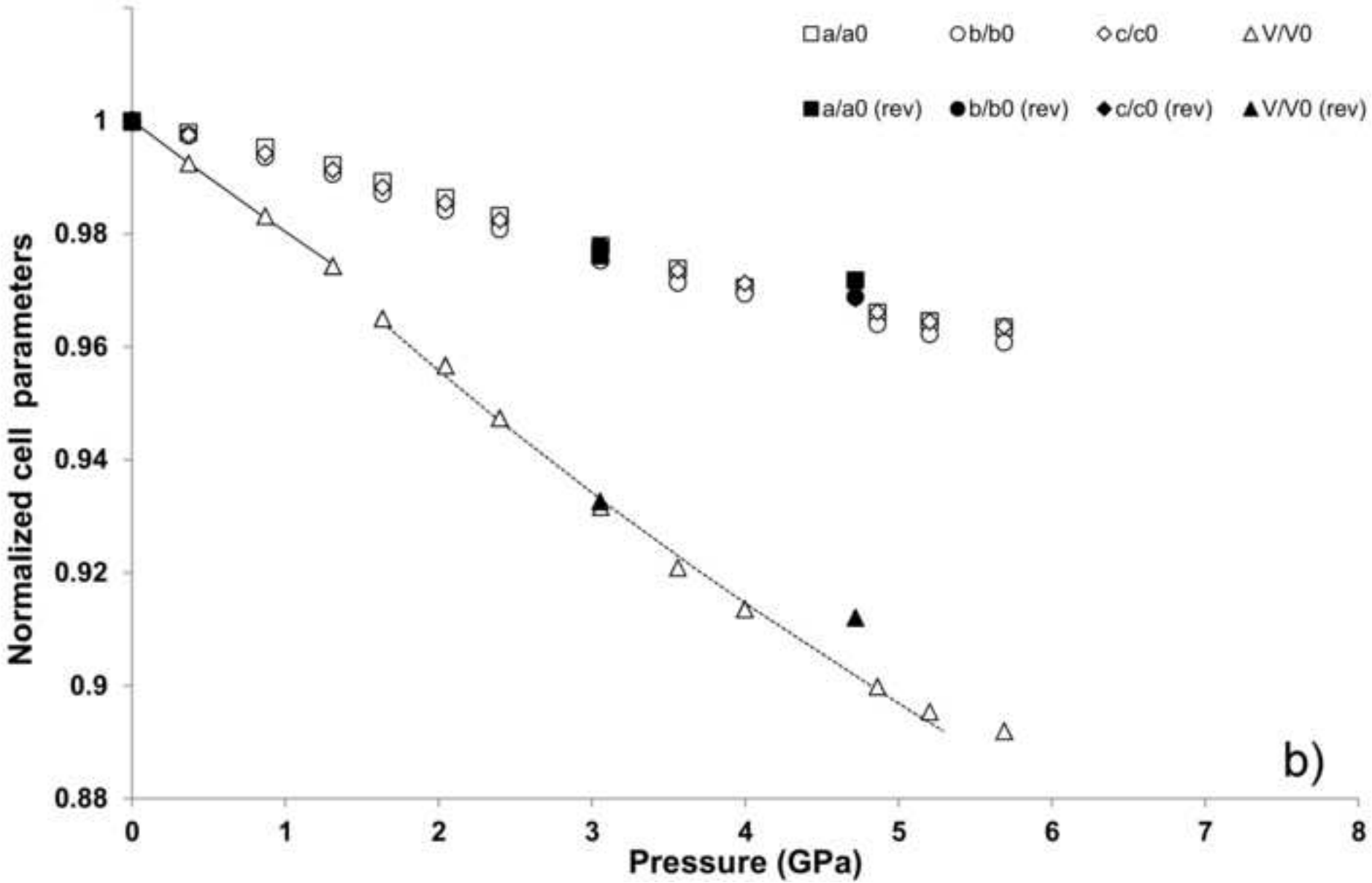

Figure6a

Click here to download high resolution image

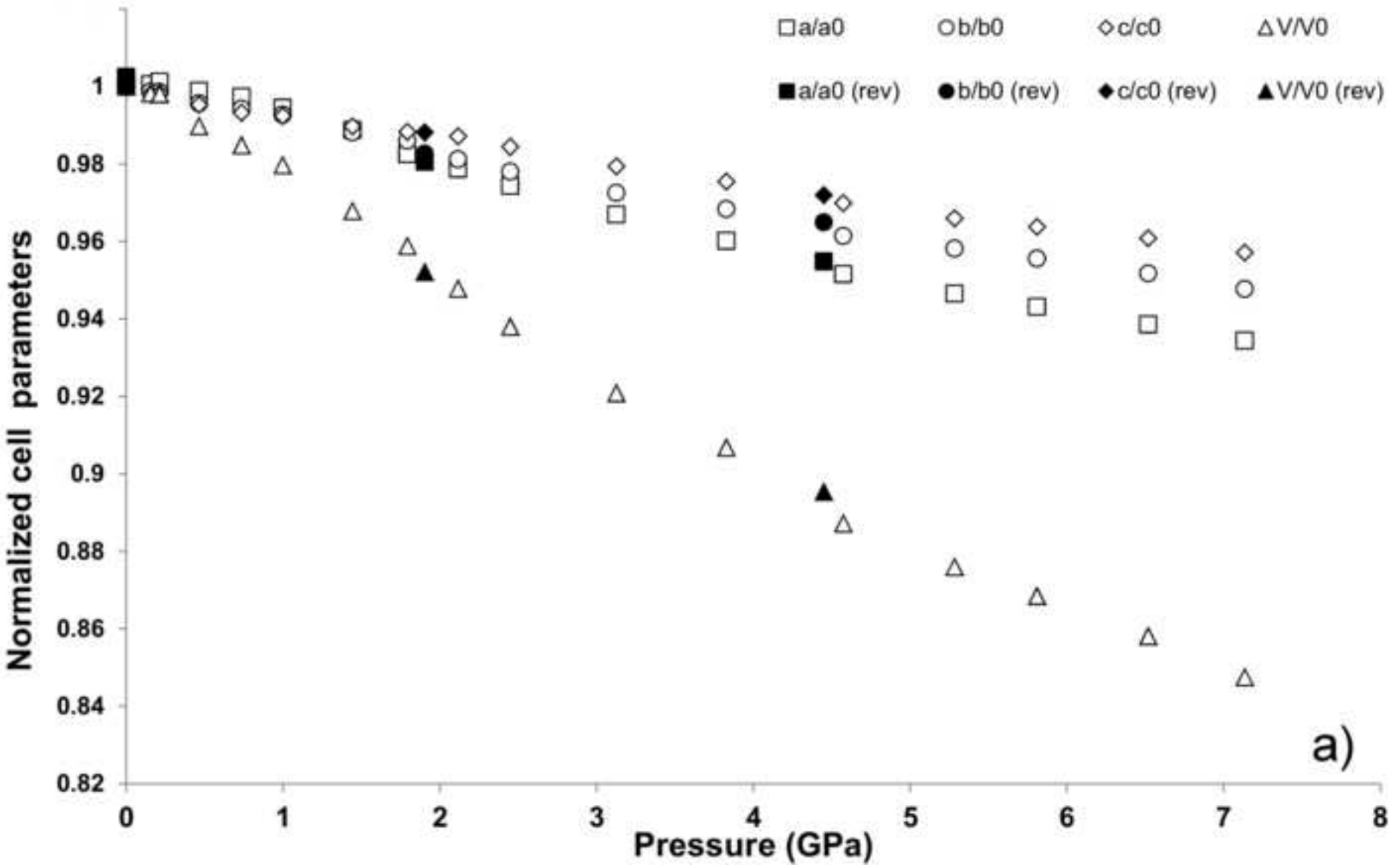

Figure6b

Click here to download high resolution image

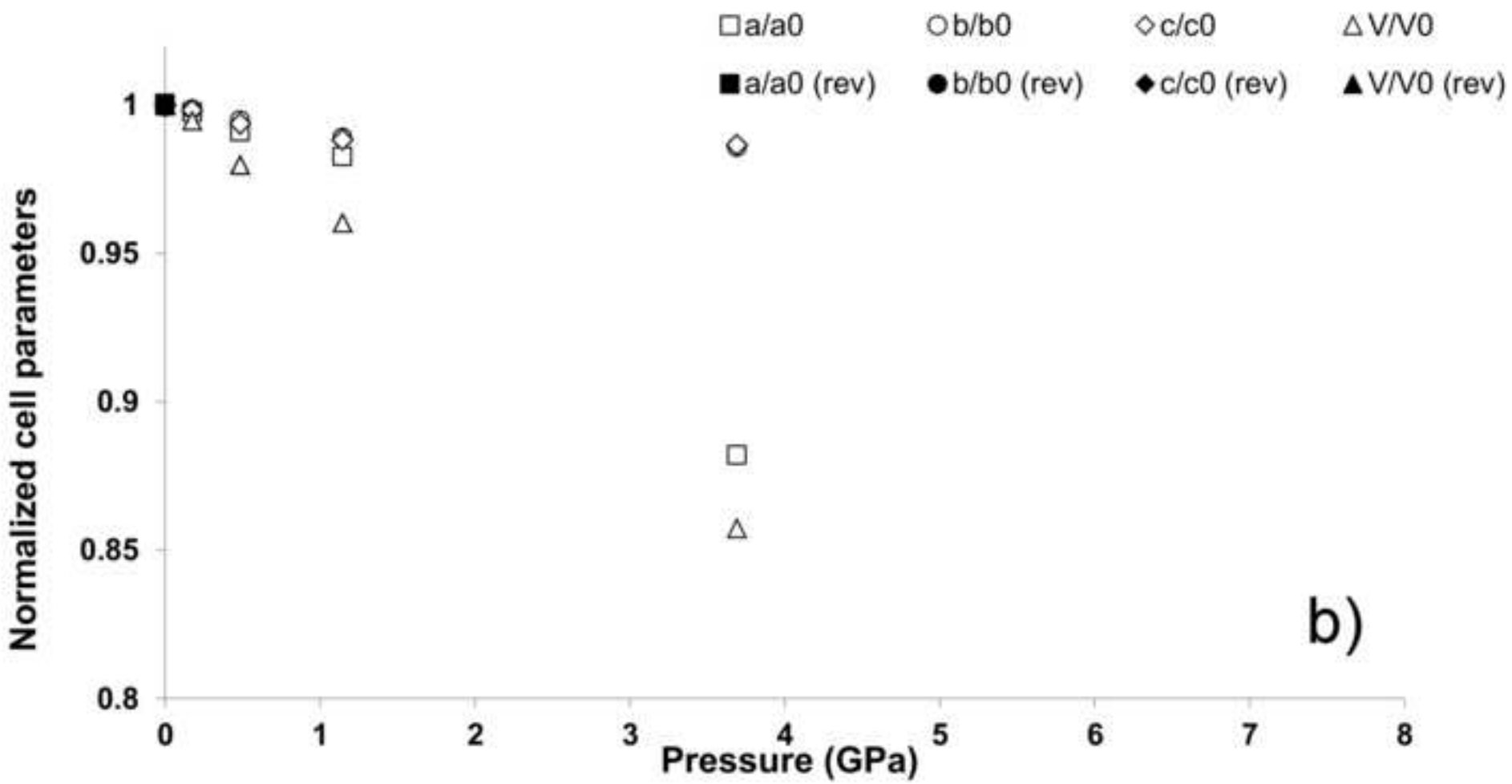

Figure7a

Click here to download high resolution image

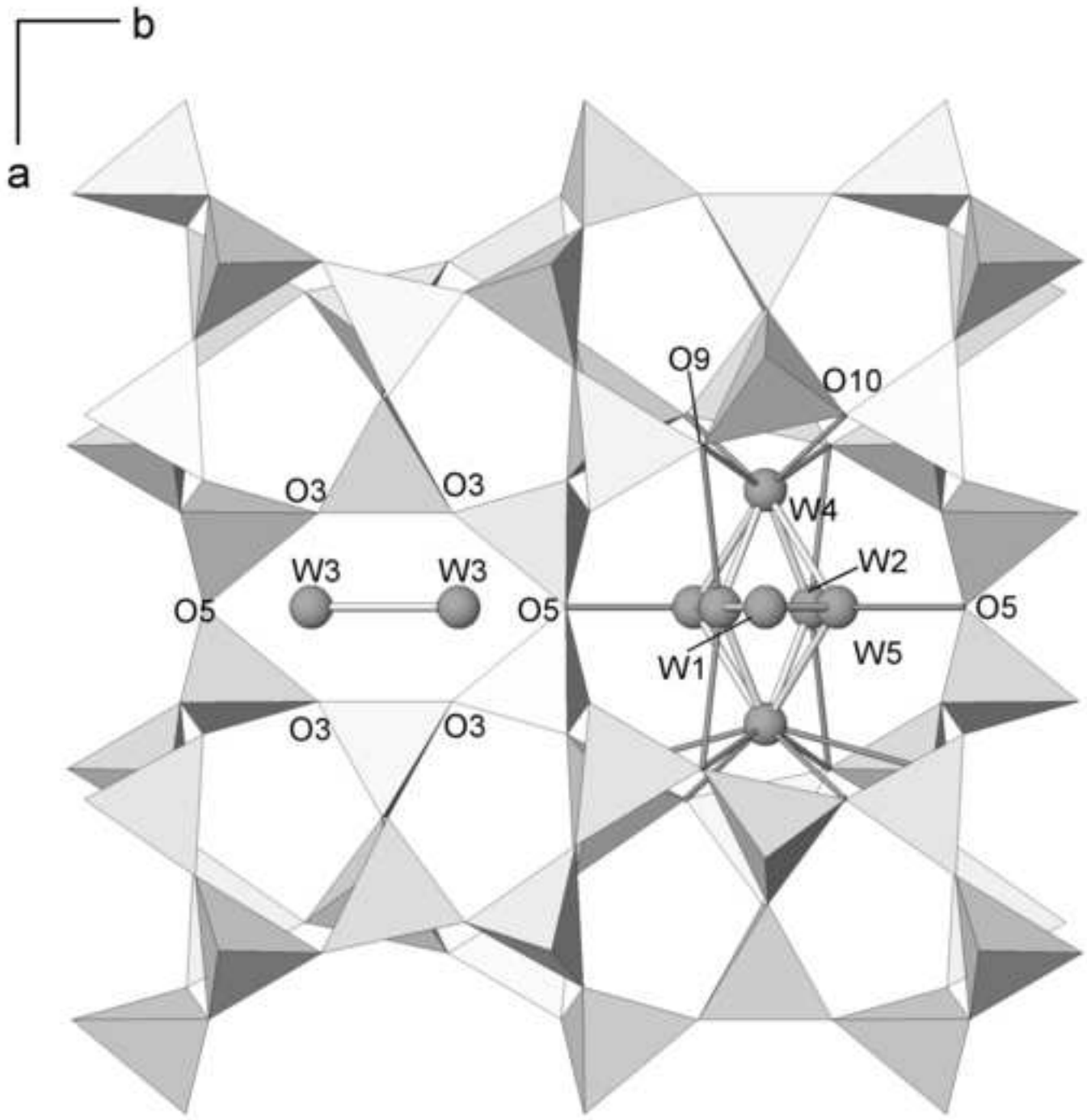

Figure7b

Click here to download high resolution image

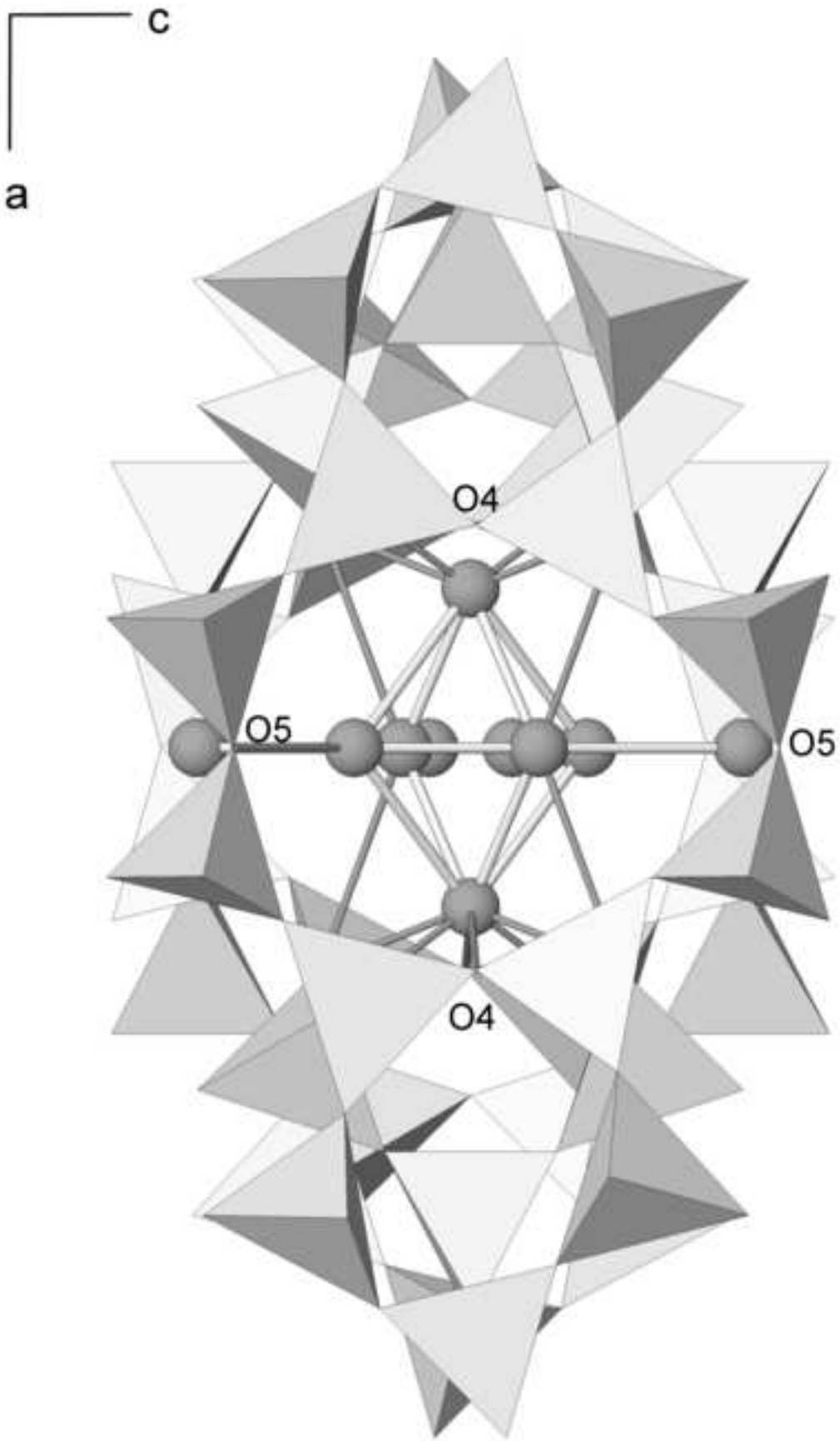

Figure8
Click here to download high resolution image

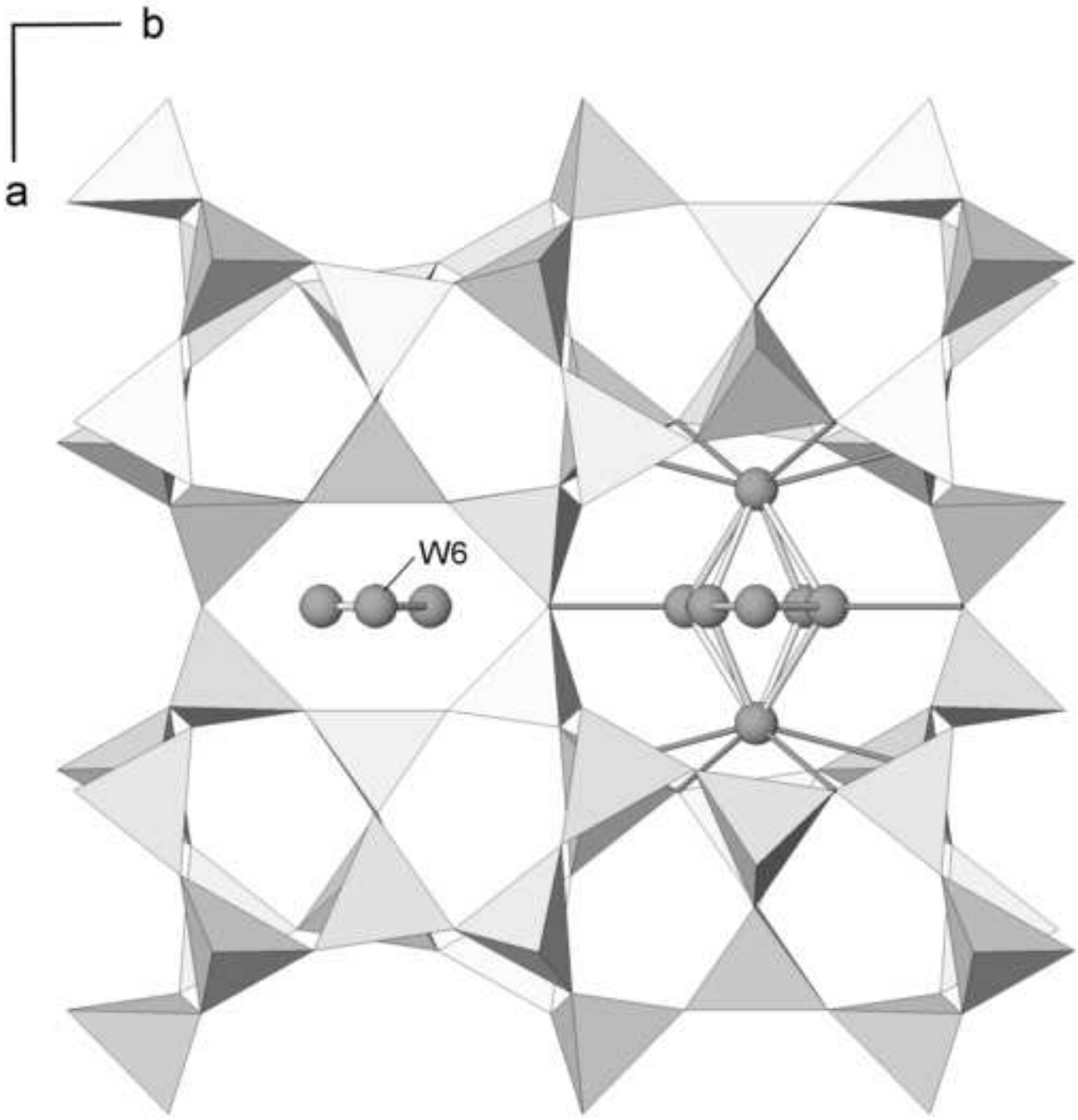

Figure10

Click here to download high resolution image

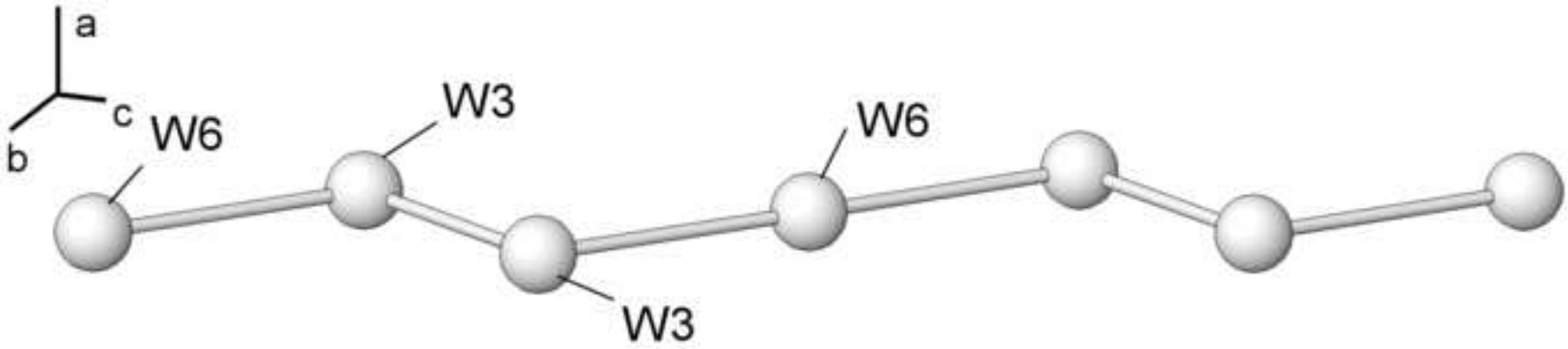

Figure 2a

Click here to download high resolution image

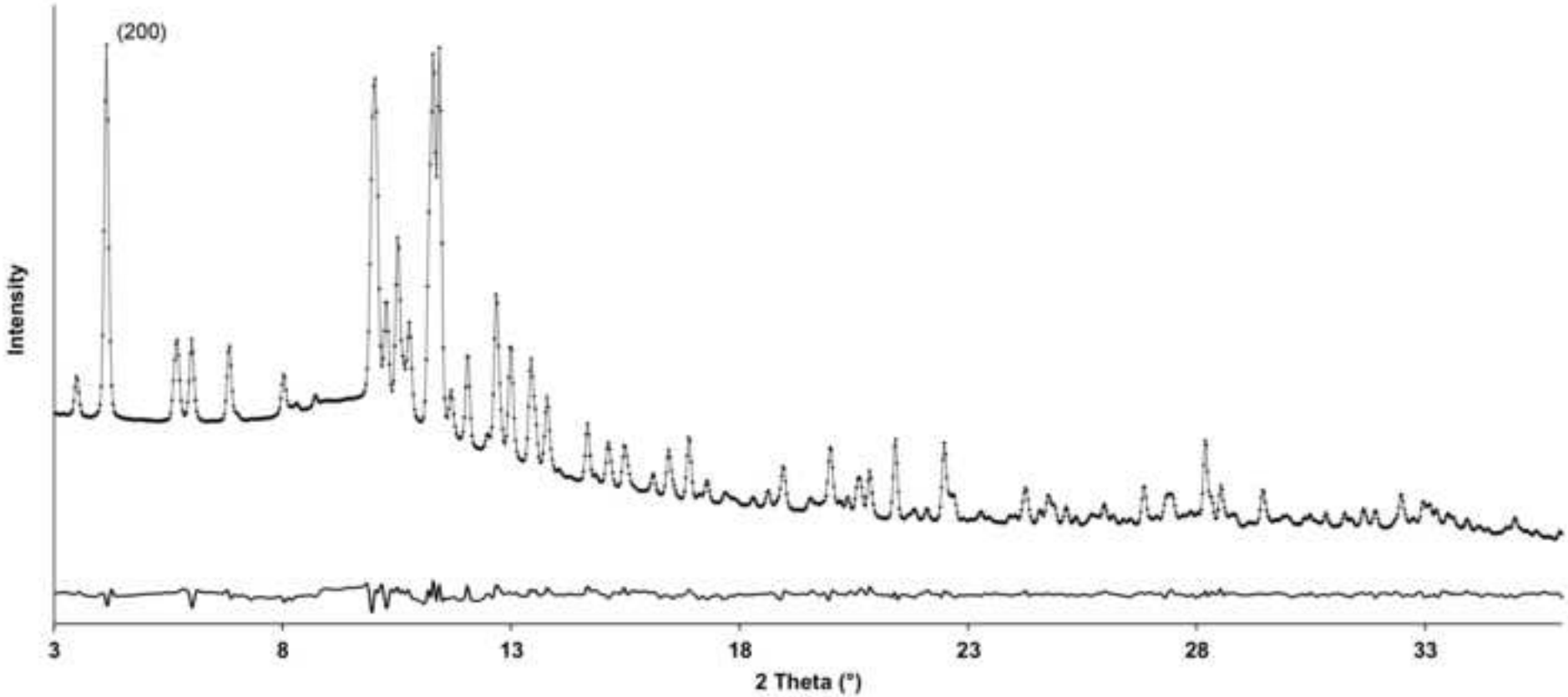

Figure 2b

Click here to download high resolution image

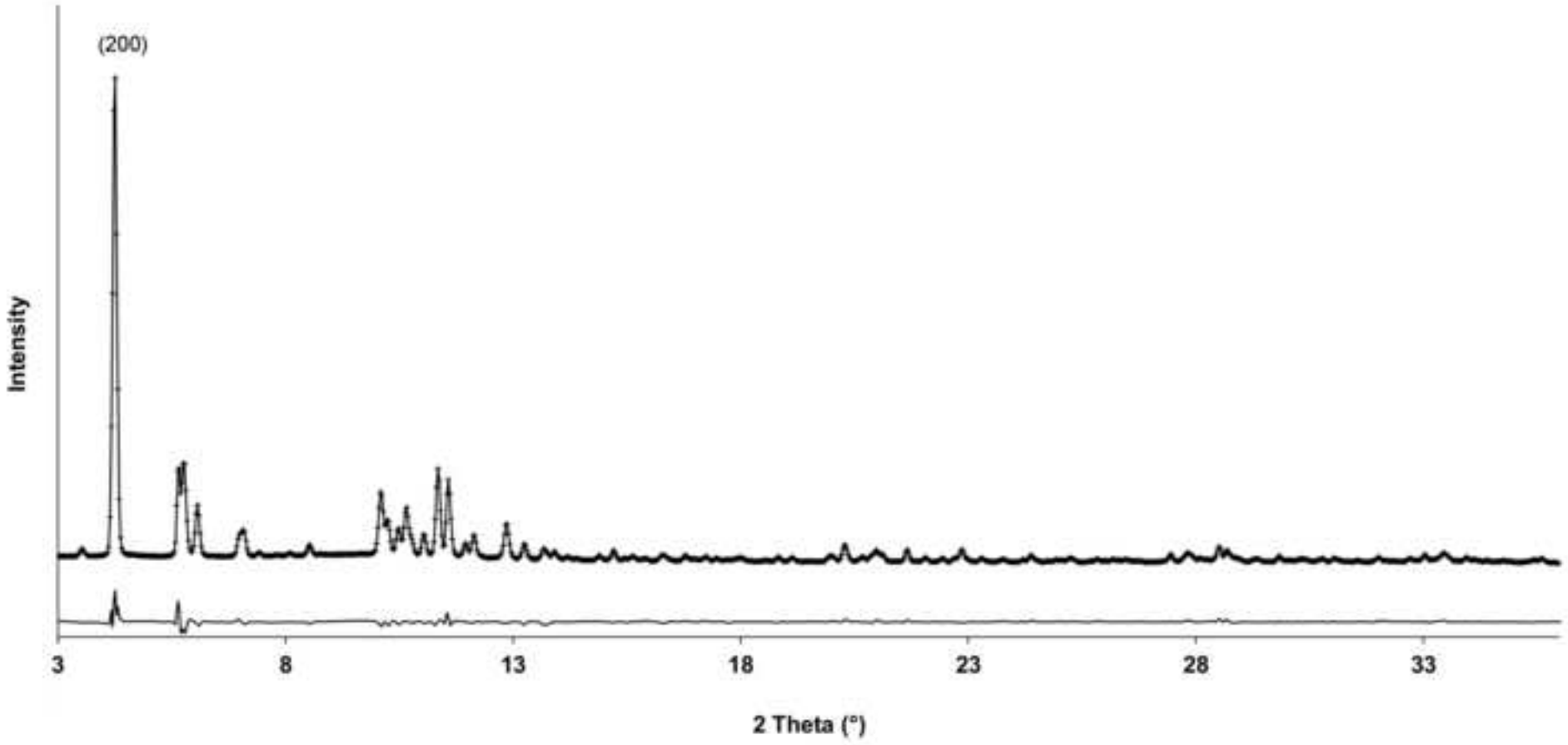

Figure 3ab

Click here to download high resolution image

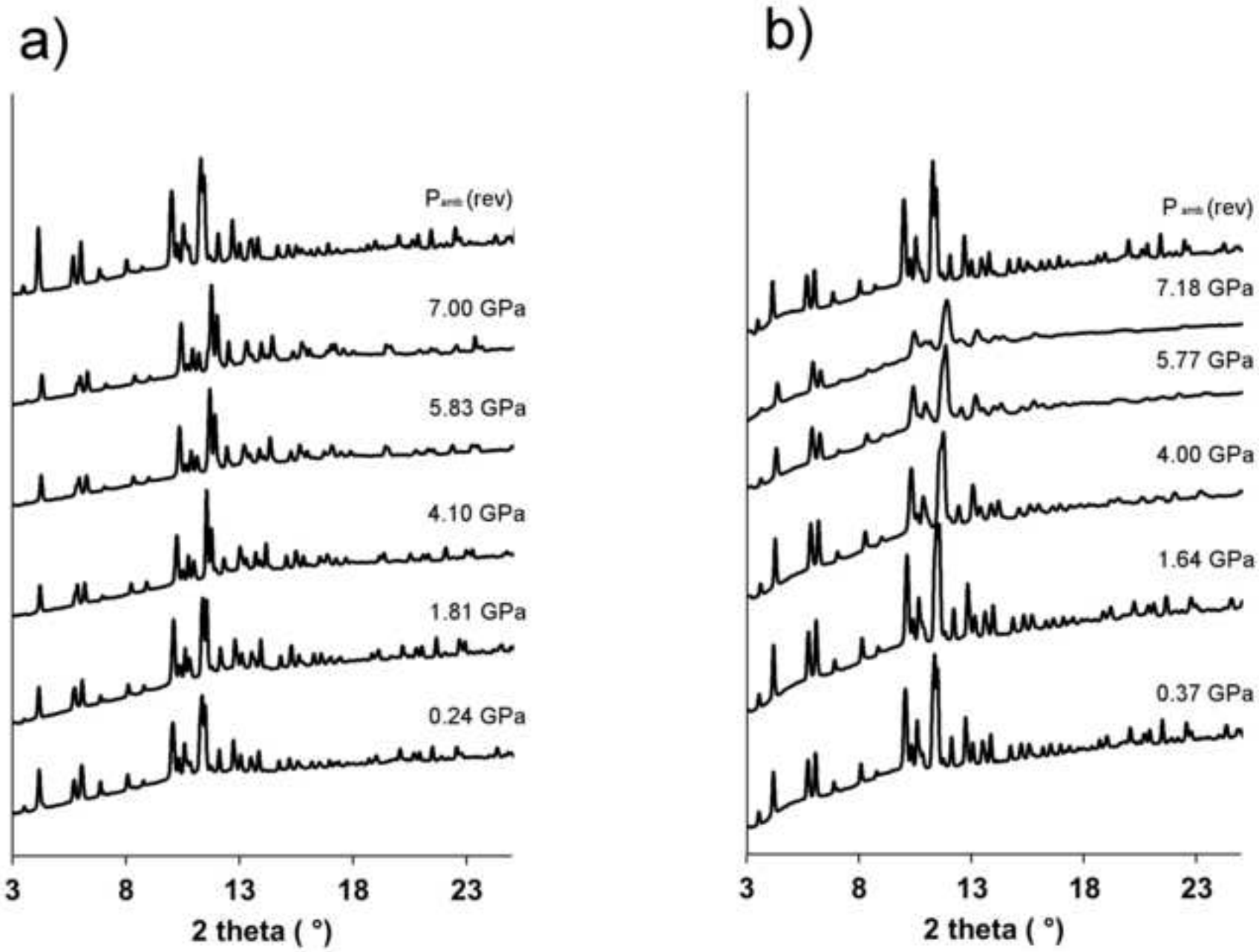

Figure 3cd

Click here to download high resolution image

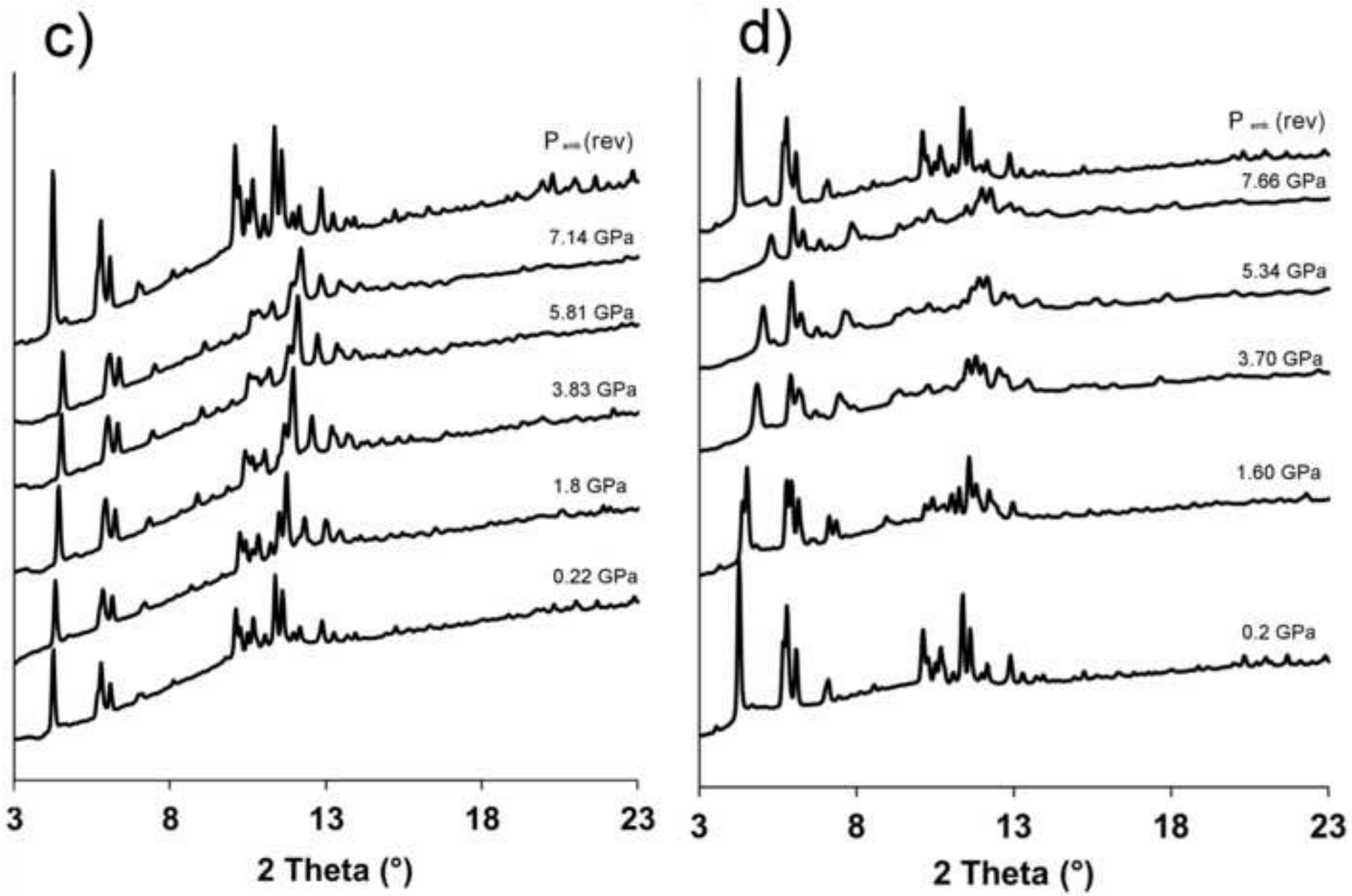

Figure 9

Click here to download high resolution image

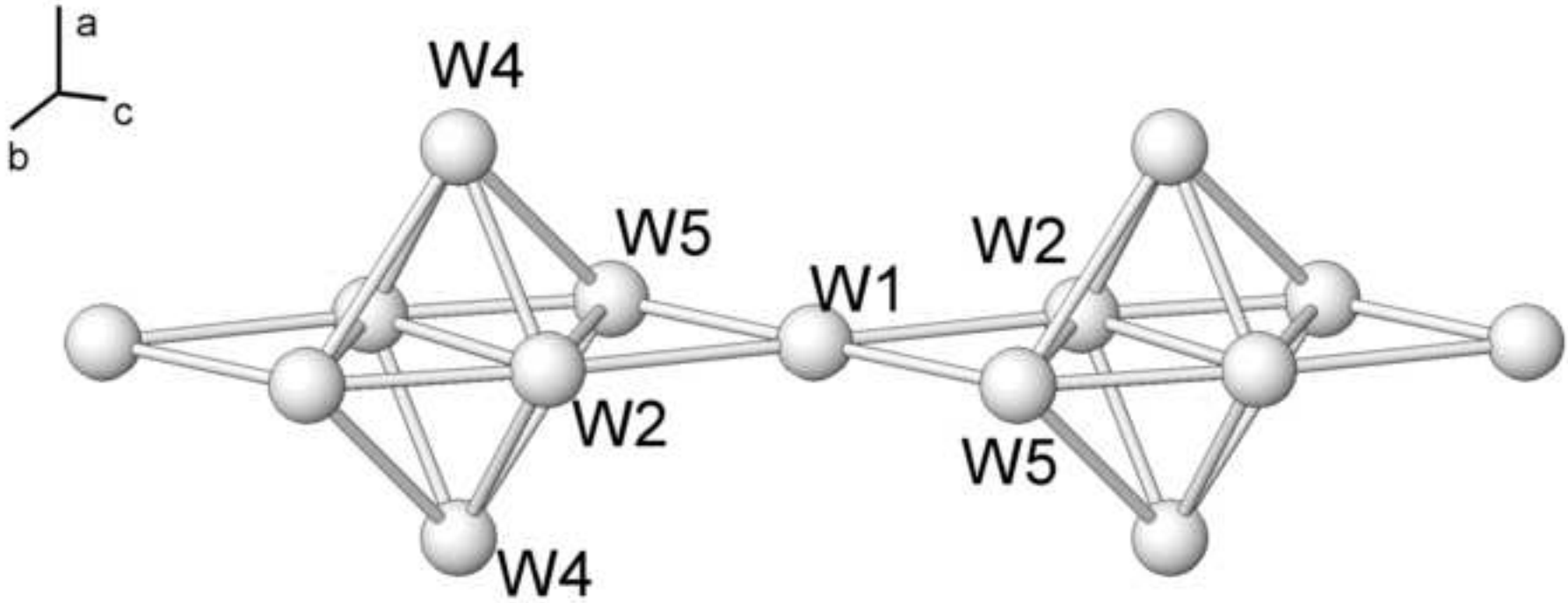

Table1

P (GPa)	P_{amb}	0.2 GPa	P_{amb}(rev)
Space Group	*Pmnn*	*Pmnn*	*Pmnn*
a **(Å)**	18.708(1)	18.699(2)	18.754(2)
b **(Å)**	14.0690(8)	14.042(1)	14.066(1)
c **(Å)**	7.4177(4)	7.3991(7)	7.4164(6)
V **(Å^3)**	1952.4(2)	1942.8(5)	1956.4(4)
xR **$_p$ (%)**	6.3	1.0	1.0
R **$_{wp}$ (%)**	4.8	1.0	1.0
R **F**2 (%)**	8.1	11.4	11.2
No. of variables	61	83	84
No. of observations	1204	1119	1121
No. of reflections	912	788	769

Table3

P_{amb}					
	x/a	**y/b**	**z/c**	**Occ**	**Uiso**
Si1	0.1570(7)	0	0	1	0.016(1)
Si2	0.2744(5)	0.0033(11)	0.2912(11)	1	0.016(1)
Si3	0.0846(4)	0.2026(7)	0.010(2)	1	0.016(1)
Si4	0.3294(6)	0.1992(9)	0.2165(18)	1	0.016(1)
Si5	0.6841(7)	0.7930(10)	0.1908(17)	1	0.016(1)
O1	0.249(1)	0	0.5	1	0.027(2)
O2	0.2015(7)	0.014(2)	0.186(2)	1	0.027(2)
O3	0.1086(7)	0.0935(9)	-0.023(4)	1	0.027(2)
O4	0.6546(8)	0.7782(12)	-0.013(2)	1	0.027(2)
O5	0	0.211(2)	0.040(5)	1	0.027(2)
O6	0.259(1)	0.250(2)	0.276(4)	1	0.027(2)
O7	0.1314(10)	0.240(2)	0.183(3)	1	0.027(2)
O8	0.8941(10)	0.741(2)	0.174(3)	1	0.027(2)
O9	0.323(1)	0.088(1)	0.236(4)	1	0.027(2)
O10	0.690(1)	0.901(11)	0.245(4)	1	0.027(2)
0.2 GPa					
	x/a	**y/b**	**z/c**	**Occ**	**Uiso**
Si1	0.147(1)	0	0	1	0.023(3)
Si2	0.278(1)	-0.001(2)	0.287(2)	1	0.023(3)
Si3	0.0716(7)	0.198(1)	-0.006(4)	1	0.023(3)
Si4	0.338(1)	0.194(1)	0.219(3)	1	0.023(3)
Si5	0.683(1)	0.780(2)	0.208(3)	1	0.023(3)
O1	0.250(2)	0	0.50	1	0.035(5)
O2	0.207(1)	-0.002(6)	0.154(4)	1	0.035(5)
O3	0.091(1)	0.088(1)	0.011(1)	1	0.035(5)
O4	0.663(1)	0.781(2)	-0.008(3)	1	0.035(5)
O5	0	0.240(2)	0.062(4)	1	0.035(5)
O6	0.264(2)	0.249(4)	0.260(10)	1	0.035(5)
O7	0.123(2)	0.238(3)	0.157(4)	1	0.035(5)
O8	0.905(1)	0.732(3)	0.169(3)	1	0.035(5)
O9	0.341(2)	0.081(2)	0.270(5)	1	0.035(5)
O10	0.690(2)	0.894(2)	0.249(7)	1	0.035(5)
W1	0	0.50	0	1.08(4)	0.22(2)
W2	0.50	0.059(2)	0.126(3)	1.11(4)	0.22(2)
W3	0.50	0.406(2)	0.076(5)	1.00(6)	0.22(2)
W4	0.115(6)	0.50	0.50	0.31(3)	0.22(2)
W5	0	0.402(2)	0.281(3)	1.09(3)	0.22(2)
P_{amb}**(rev)**					
	x/a	**y/b**	**z/c**	**Occ**	**Uiso**
Si1	0.150(1)	0	0	1	0.024(2)
Si2	0.2759(9)	-0.003(2)	0.292(2)	1	0.024(2)
Si3	0.0757(7)	0.198(1)	-0.003(4)	1	0.024(2)
Si4	0.336(1)	0.196(1)	0.214(3)	1	0.024(2)
Si5	0.683(1)	0.785(2)	0.202(3)	1	0.024(2)
O1	0.244(2)	0	0.50	1	0.025(4)
O2	0.203(1)	0.002(6)	0.167(3)	1	0.025(4)
O3	0.103(1)	0.094(1)	-0.013(9)	1	0.025(4)
O4	0.659(1)	0.786(2)	-0.006(3)	1	0.025(4)
O5	0	0.228(2)	0.051(5)	1	0.025(4)
O6	0.265(2)	0.256(3)	0.268(8)	1	0.025(4)
O7	0.119(2)	0.242(3)	0.169(4)	1	0.025(4)
O8	0.901(2)	0.729(3)	0.161(4)	1	0.025(4)
O9	0.339(2)	0.082(2)	0.263(6)	1	0.025(4)
O10	0.682(2)	0.897(2)	0.253(7)	1	0.025(4)
W1	0	0.50	0	1.11(5)	0.27(2)
W2	0.50	0.063(2)	0.1181(34)	1.12(5)	0.27(2)
W3	0.50	0.429(2)	0.100(4)	1.13(3)	0.27(2)
W4	0.1153(9)	0.50	0.50	0.30(3)	0.27(2)
W5	0	0.407(2)	0.2865(30)	0.96(8)	0.27(2)
W6	0	0	0	0.15(4)	0.27(2)

Table2

Mon-FER (m.e.w)					
P (GPa)	**a(Å)**	**b(Å)**	**c(Å)**	**V(Å3)**	**β (°)**
P_{amb}	**19.2119(9)**	**14.1438**(5)	**7.5048**(2)	**2039.3**(1)	
0.001	19.187(3)	14.132(1)	7.4980(7)	2033.1(5)	
0.10	19.184(2)	14.122(2)	7.4936(9)	2030.2(6)	
0.24	19.175(2)	14.111(2)	7.4884(8)	2026.2(5)	
0.41	19.169(3)	14.092(2)	7.479(1)	2020.2(7)	
0.80	19.145(3)	14.069(2)	7.463(1)	2010.4(8)	
1.42	19.122(4)	14.041(4)	7.437(1)	1995.5(8)	
1.81	19.092(3)	14.033(2)	7.419(1)	1984.4(8)	
2.46	19.022(5)	13.961(3)	7.373(2)	1957(1)	
3.10	18.950(5)	13.910(3)	7.335(2)	1933(1)	
4.10	18.823(5)	13.820(3)	7.278(2)	1893(1)	
4.91	18.722(5)	13.759(4)	7.236(2)	1864(1)	
5.83	18.611(7)	13.686(5)	7.183(2)	1830(1)	
6.45	18.555(7)	13.647(4)	7.162(2)	1808(1)	
7.00	18.468(8)	13.606(6)	7.130(2)	1791(1)	
5.45(rev)	18.646(6)	13.732(4)	7.200(2)	1843(1)	
3.61(rev)	18.901(6)	13.877(4)	7.306(2)	1916(1)	
P_{amb} (rev)	19.204(3)	14.130(1)	7.4977(8)	2034.6(6)	
Mon-FER (s.o.)					
P_{amb}	**19.2119(9)**	**14.1438**	**7.5048**	**2039.3**(1)	
0.37	19.172(7)	14.107(3)	7.486(2)	2024(1)	
0.87	19.122(7)	14.053(3)	7.462(1)	2005(1)	
1.31	19.062(9)	14.010(4)	7.440(2)	1987(1)	
1.64	19.005(7)	13.962(3)	7.417(2)	1968(1)	
2.05	18.95(1)	13.920(4)	7.396(2)	1951(2)	
2.40	18.889(8)	13.872(4)	7.373(2)	1932(1)	
3.06	18.787(9)	13.794(4)	7.335(2)	1900(1)	
3.56	18.709(9)	13.738(4)	7.306(2)	1878(1)	
4.00	18.646(9)	13.711(4)	7.289(2)	1863(1)	
4.86	18.56(1)	13.634(5)	7.251(2)	1835(2)	
5.20	18.53(1)	13.609(4)	7.238(2)	1826(2)	
5.77	18.51(1)	13.589(6)	7.232(3)	1819(2)	
4.72(rev)	18.67(1)	13.703(5)	7.269(4)	1860(1)	
3.05(rev)	18.753(9)	13.831(4)	7.335(2)	1902(1)	
P_{amb} (rev)	19.211(7)	14.146(3)	7.503(1)	2039(1)	
Si- FER (m.e.w.)					
P_{amb}	18.708(1)	14.0690(8)	7.4177(4)	1952.4(2)	
0.16	18.717(3)	14.050(1)	7.4030(7)	1948.8(5)	
0.22	18.730(3)	14.049(2)	7.405(1)	1948.6(3)	
0.47	18.687(3)	14.008(1)	7.3822(7)	1932.4(5)	
0.74	18.658(3)	13.988(2)	7.3675(8)	1922.8(5)	
1.00	18.605(4)	13.966(2)	7.361(1)	1912.8(5)	
1.45	18.497(5)	13.902(2)	7.348(1)	1889.7(8)	
1.80	18.380(5)	13.872(2)	7.341(1)	1872(1)	89.71(2)

2.12	18.310(2)	13.804(1)	7.3220(5)	1850.6(4)	89.59(1)
2.45	18.227(2)	13.760(1)	7.3022(5)	1831.4(4)	89.50(1)
3.13	18.090(2)	13.682(1)	7.2647(4)	1797.9(3)	89.41(1)
3.83	17.962(2)	13.623(1)	7.2354(5)	1770.4(3)	89.31(1)
4.58	17.801(3)	13.526(2)	7.1941(7)	1732.1(5)	89.37(1)
5.3	17.708(3)	13.480(1)	7.1652(6)	1710.2(4)	89.34(1)
5.81	17.643(2)	13.444(1)	7.1491(5)	1695.6(3)	89.34(1)
6.52	17.559(2)	13.389(1)	7.1269(5)	1675.3(4)	89.36(1)
7.14	17.480(4)	13.333(2)	7.100(8)	1654.7(6)	89.40(1)
4.5 (rev)	17.862(3)	13.576(1)	7.2098(7)	1748.1(5)	89.27(1)
1.91rev)	18.344(2)	13.825(1)	7.3298(4)	1858.9(4)	89.63(1)
P_{amb} (rev)	18.754(2)	14.066(1)	7.4164(6)	1956.5(4)	
Si- FER (s.o.)					
Pamb	18.708(1)	14.0690(8)	7.4177(4)	1952.4(2)	
0.10	18.663(6)	14.050(3)	7.405(1)	1942(1)	
0.49	18.541(6)	13.998(2)	7.371(1)	1913(1)	
1.15	18.384(8)	13.915(3)	7.331(2)	1875(1)	
3.60*	16.502(5)	13.870(3)	7.318(2)	1674.2(9)	88.28(3)
Pamb (rev)	18.719(7)	14.060(3)	7.416(2)	1952(1)	

Table4

		P_{amb}		0.2 Gpa		P_{amb}(rev)	
Si1-	**O2**	1.626(8)	x2	1.608(8)	x2	1.600(12)	x2
	O3	1.606(8)	x2	1.616(8)	x2	1.593(12)	x2
Si2-	**O1**	1.619(8)		1.662(10)		1.655(14)	
	O2	1.588(9)		1.645(10)		1.645(14)	
	O9	1.621(10)		1.657(11)		1.69(2)	
	O10	1.545(10)		1.617(11)		1.64(2)	
Si3-	**O3**	1.618(9)		1.603(11)		1.552(14)	
	O5	1.603(8)		1.549(10)		1.534(14)	
	O7	1.641(10)		1.641(11)		1.63(2)	
	O8	1.625(10)		1.613(11)		1.61(2)	
Si4-	**O4**	1.568(11)		1.599(11)		1.552(14)	
	O6	1.570(10)		1.609(11)		1.534(14)	
	O8	1.573(10)		1.592(11)		1.60(2)	
	O9	1.577(10)		1.632(11)		1.61(2)	
Si5-	**O4**	1.626(10)		1.641(11)		1.61(2)	
	O6	1.538(10)		1.594(11)		1.61(2)	
	O7	1.550(10)		1.623(11)		1.65(2)	
	O10	1.574(11)		1.636(11)		1.61(2)	
W1-	**W2**			2.90(3)	x2	2.97(3)	x2
	W5			2.50(9)	x2	2.50(1)	x2
W2-	**O9**			3.17(2)	x2		
	W1			2.90(3)		2.97(3)	
	W2			2.50(1)		2.50(2)	
	W4			2.50(9)	x2	2.50(1)	x2
	W5			2.61(4)		2.50(4)	
	W5			2.32(4)		2.31(5)	
W3-	**W3**			2.88(6)		2.49(6)	
	W6					3.13(4)	
W4-	**O4**			3.20(4)	x2	3.131(5)	x2
	O9			2.44(4)	x2	2.423(6)	x2
	O10			2.75(6)	x2	2.690(8)	x2
	W2			2.50(9)	x2	2.49(1)	x2
	W5			3.04(3)	x2	2.98(2)	x2
W5-	**O5**			2.79(4)		3.07(4)	
	W1			2.499(9)		2.50(1)	
	W2			2.61(4)		2.50(4)	
	W2			2.32(4)		2.31(5)	
	W4			3.04(3)	x2	2.98(2)	x2
W6-	**O3**					2.342(2)	
	W3					3.13(4)	X2